Universidade de Aveiro
2023

Hugo Coutinho Gomes

Sensores em fibra ótica baseados em grafeno induzido por laser para potencial aplicação em aquacultura

Fiber optic sensors based on laser-induced graphene for potential application in aquaculture

"*You have power over your mind – not outside events. Realize this, and you will find strength.*"

— Marcus Aurelius

Universidade de Aveiro
2023

Hugo Coutinho Gomes

Sensores em fibra ótica baseados em grafeno induzido por laser para potencial aplicação em aquacultura

Fiber optic sensors based on laser-induced graphene for potential application in aquaculture

Dissertação apresentada à Universidade de Aveiro para cumprimento dos requisitos necessários à obtenção do grau de Mestre em Engenharia Física, realizada sob a orientação científica do Doutor Carlos Alberto Ferreira Marques, Professor principal do Departamento de Física da Universidade de Aveiro, e do Doutor Nuno Miguel Franco dos Santos, Investigador de Pós-doutoramento do Departamento de Física da Universidade de Aveiro.

Este trabalho foi desenvolvido no âmbito do projeto i3N, UIDB/50025/2020 & UIDP/50025/2020 & LA/P/0037/2020, e do projeto DigiAqua PTDC/EEI-EEE/0415/2021 financiados por fundos do FEDER através do programa COMPETE 2020 e da FCT – Fundação portuguesa para a Ciência e Tecnologia.

FCT Fundação para a Ciência e a Tecnologia
MINISTÉRIO DA CIÊNCIA, TECNOLOGIA E ENSINO SUPERIOR

i3N INSTITUTE FOR NANOSTRUCTURES, NANOMODELLING AND NANOFABRICATION
RESEARCH, INNOVATION AND ENGINEERING APPLICATIONS

DIGIAQUA
DIGITIZING AQUACULTURE

Dedico este trabalho aos meus pais, irmão e a toda a minha família que sempre me apoiou.

o júri / the jury

presidente / president

Prof. Doutora Maria do Rosário Pimenta Correia
Professor Associado do Departamento de Física da Universidade de Aveiro

vogais / examiners committee

Prof. Doutor José Luís Campos de Oliveira Santos
Professor Catedrático do Departamento de Física e Astronomia da Universidade do Porto

Prof. Doutor Carlos Alberto Ferreira Marques
Investigador Principal do Departamento de Física da Universidade de Aveiro

agradecimentos / acknowledgements

Quero agradecer, desde já, toda a disponibilidade, acompanhamento, e conhecimentos transmitidos pelo Doutor Carlos Alberto Ferreira Marques e pelo Doutor Nuno Miguel Franco dos Santos na orientação e co-orientação deste trabalho, respetivamente.

Quero agradecer à Doutora Ana Catarina Fernandes Moreirinha pela disponibilidade na aquisição dos espetros de ATR-FTIR e ao Doutor António José Silva Fernandes pela transmissão de conhecimentos e à aquisição de espetros de Raman.

Quero agradecer ao Luis Martins pela ajuda que me deu no inicio deste trabalho e ao Liu Xuecheng pelo acompanhamento na sintese da nanopartículas de ouro, na funcionalização do cortisol e por ter ficado no laboratório comigo fora de horas. Agradeço também ao João Marques pela disponibilização da curva de calibração do laser. Agradeço também à Clara Rodrigues pela revisão do documento.

Quero agradecer ao Chico, ao Nuno, ao Preizal, ao Rama, ao Miguel, ao Tomás e ao João que tiveram de me aturar ao longo deste cinco anos. Agradeço também à Verónica e à Ana por me terem escolhido (por algum motivo que eu não sei) como patrão. Agradeço à Sofia por ser a melhor pessoa que Aveiro me deu e por todo o apoio que me dá. Isto também é um bocadinho vosso.

Por fim, o agradecimento mais especial é para a Cristina, para o Augusto, para o Tomás e para o resto da minha familia pelo apoio incondicional, pela paciência e pelo carinho.

Palavras Chave

Sensores de fibra ótica, Poliimida, Cavidades de Fabry-Perrot, Grafeno induzido por laser (LIG), Cortisol.

Resumo

O cortisol e amonia são indicadores chave para o desenvolvimento eficiente e saudável de culturas para a aquacultura. Tendo isto em vista, este trabalho propõe a aplicação de um sensor baseado em grafeno induzido por laser (LIG) para a potencial quantificação e monitorização de cortisol e amonia em águas de aquacultura. Os sensores desenvolvidos foram criados a partir do princípio da cavidade de Fabry-Pérot. As cavidades foram preenchidas com poliimida e em alguns casos foi lhes misturadas nano partículas de ouro. Os interferómetros foram testados ao estiramento, temperatura e índice de refração, observando-se um aumento da sensibilidade ao índice de refração devido à adição das nanoparticulas. O próximo passo, passou por avaliar os melhores parâmetros do laser para criar uma camada de LIG à volta dos interferómetros. Observou-se que para uma potência de 10% e uma velocidade de inscrição de 100 mm/s, o LIG formado apresentava bastante porosidade, era bastante homogéneo e tinha uma textura folhosa. Com recurso a um laser de CO_2 pulsado, a poliimida foi então irradiada e transformada em LIG, criando uma segunda cavidade dentro do interferómetro. Devido a isto, a resposta espetral dos interferómetros assemelhou-se ao efeito de Vernier. O comportamento ao índice de refração foi novamente avaliado, mostrando melhorias na sensibilidade até 153 vezes devido à criação da cavidade de LIG. Os interferómetros foram então funcionalizados para terem uma afinidade ao cortisol, sendo que esta é uma abordagem inovadora, obtendo sensibilidades de -4.1$\pm$0.2 nm/log(ng/mL) e -34$\pm$5 nm/log(ng/mL) para dois interferómetros sem e com nano partículas de ouro misturadas na poliimida, respetivamente. O aumento da sensibilidade nestes interferómetros é justificada com a presença destas nano partículas de ouro na poliimida. Foi também possível observar que os sensores são imunes à interferência de substâncias como a glucose, sacarose, frutose e ácido ascórbico. No que toca à detenção de amónia, obtiveram-se sensibilidades de -80$\pm$10 nm/ppm para sensores onde foi misturada oxazina 170 perclorato na poliimida.

Keywords Fiber optic sensors, Polyimide, Fabry-Perrot cavities, Laser-induced graphene (LIG), Cortisol.

Abstract Cortisol and ammonia are key indicators for the efficient and healthy development of aquaculture cultures. With this in mind, this work proposes the application of a laser-induced graphene (LIG) based sensor for the potential quantification and monitoring of cortisol and ammonia in aquaculture waters. The developed sensors were created from the Fabry-Pérot cavity principle. The cavities were filled with polyimide and in some cases mixed with gold nanoparticles. The interferometers were tested for strain, temperature, and refractive index, being observed an increase in the sensitivity to the refractive index due to the addition of the nanoparticles. The next step was to evaluate the best laser parameters to create a layer of LIG around the interferometers. It was observed that for a power of 10% and an inscription speed of 100 mm/s, the formed LIG was quite porous, homogeneous, and had a leafy texture. Using a pulsed CO_2 laser, the polyimide was then irradiated and transformed into LIG, creating a second cavity within the interferometer. Due to this, the spectral response of the interferometers resembled the Vernier effect. The refractive index behavior was again evaluated, showing improvements in sensitivity up to 153 times due to the creation of the LIG cavity. The interferometers were then functionalized to achieve an affinity to cortisol, this being a novel approach, obtaining sensitivities of -4.1$\pm$0.2 nm/log(ng/mL) and -34$\pm$5 nm/log(ng/mL) for two interferometers without and with gold nanoparticles mixed into the polyimide, respectively. The increased sensitivity in these interferometers is justified by the presence of these gold nanoparticles in the polyimide. It was also possible to observe that the sensors are immune to interference from substances such as glucose, sucrose, fructose, and ascorbic acid. Regarding ammonia arrest, sensitivities of -80$\pm$10 nm/ppm were obtained for sensors where oxazine 170 perchlorate was mixed in the polyimide.

Contents

List of Figures

List of Tables

Acronyms and Abbreviations

MPTMS	(3-Mercaptopropyl)trimethoxysilane
MUA	11-Mercaptoundecanoic acid
ATR-FTIR	Attenuated Total Reflectance Fourier-Transform Infrared Spectroscopy
BSE	Backscattered Electron
DNA	Deoxyribonucleic Acid
DI water	dionized water
EDS	Energy Dispersive X-ray Spectroscopy
EDC	ethylcarboiimide hydrochlorine
FPI	Fabry-Perrot Interferometer
FBG	Fiber Bragg Grating
FOS	Fiber Optic Sensor
FTIR	Fourier-Transform Infrared Spectroscopy
FSR	Free Spectral Range
FWHM	Full Width at Half Maximum
AuNPs	Gold Nanoparticles
GO	Graphene Oxide
IR	Infra-Red
LIG	Laser Induced Graphene
LSPR	Localized Surface Plasmon Resonance
MZI	Mach-Zender Interferometers
MI	Michelson Interferometers
MLG	Multi Layer Graphene
MMF	Multi-Mode Fiber
NHS	N-hydroxysuccinimide
NA	Numerical Aperture
PBS	phosphate-buffered saline
PI	Polyimide
RI	Refravtive Index
SI	Sagnac Interferometers
SEM	Scanning Electron Microscope
SE	Secundary Electron
SLG	Single Layer Graphene
SMF	Single-Mode Fiber
SPR	Surface Plasmon Resonance
TFBG	Tilted Fiber Bragg Grating
TIR	Total Internal Reflection
UV	Ultra-Violet
VE	Vernier Effect

— 1 —

Introduction

1.1 Motivation

As quickly as the global population increased, the production and consumption of food increased as well. Nowadays, the world produces more than 340 million tonnes of food per year, resulting in a 1303 billion market of meat, poultry, and seafood [1]. Asia is the major supplier of this market, from where, in 2020, 40% of the world's production came, followed by Europe (19,3%) and North America (19,1%). Worldwide, fish and seafood represented, in 2019, nearly 32% of the total food consumption. This number varies from country to country, for example, in Portugal, each person ate 57 kg of fish and seafood on average in that year, which represents almost 40% of Portugal's total food consumption [2]. This constitutes a huge pressure on the sea's resources, indeed the consumption of fish and seafood is now four times larger than it was 50 years ago, leading to a situation where the rate at which fish are caught is greater than the rate at which they reproduce sustainably [3]. Catch limits were imposed to preserve species and their wild stock, and sustainable ways to collect fish were being increasingly popular. For this reason, aquaculture grew exponentially in such a way that in 2015, 53% of fish and seafood came from aquaculture [3].

One of the biggest advantages of aquaculture is the high quantity of culture per volume unity resulting in a higher culture density when compared with other methods. This enables a more efficient and controlled way to monitor the crop and its environment. However, this intensive practice produces a problem related to water pollution, the high quantity of living organisms in such small spaces results in a dangerous accumulation of nutrients, solid wastes, antibiotics, heavy metals, or pesticides [4] [5] [6]. In the first instance, this can affect the quality and welfare of crops due to contaminants accumulation in fish's body systems but also cause illnesses in final consumers who eat these fishes. Ammonia accumulation represents one of these pollution problems, its presence is related to water eutrophication as a result of bacterial activity. For example, organic matter like food and excretions as a result of a crop's metabolic processes are transformed into ammonia by these bacterias [7] [8]. Besides eutrophication, ammonia can be oxidated to nitrate or nitrite by microorganisms present in waters [7] [9], this process is called nitritification and can be harmful to crops due to its toxic

nature when occurring in high concentrations and due to the reduction of oxygen concentration in water [9]. Some of the consequences of high ammonia concentration are: reduced growth and feed intake, haematological/structural/morphological alterations, apoptosis, and reduction of immunocompetence [9]. To avoid these problems, some regulatory entities such as the Food and Agriculture Organization (FAO) advise that ammonia levels should not exceed 20 ng/mL or 200 ppb [10]. So it's important to monitor and control the concentration of ammonia in aquaculture waters as it plays an important role in the quality, and health of the crop and, in the last instance, in the health of consumers. Furthermore, like human beings, fishes have as well the cortisol hormone which is highly related to stress but also plays important roles in blood pressure control, cardiovascular balance, and several other physiological functions. In aquaculture waters, high levels of cortisol (cortisol concentration can reach up to 10 ng/ml [11]) can be an indication of overcrowding, poor water quality, changes in the ecosystem conditions, diseases, or infections [12][13]. These conditions affect directly the crop as some fishes end up dying, and others end up feeding less resulting in a decrease in production efficiency, quality, and price of fish. This shows the importance of monitoring the cortisol concentration in aquaculture waters for the welfare of fish and for producers.

Normally, techniques such as mass spectrometry, high-performance liquid chromatography, or colorimetric analysis are used for the quantification of cortisol and ammonia. These must be performed by specialized personnel and require expensive equipment and a long transport of the sample to the laboratories. This is seen as a disadvantage compared to other recent technologies.

Optical fiber sensors have proven useful for quantifying ammonia and cortisol in aquaculture waters, it has been shown to be faster, smaller, and simpler technologies than traditional techniques. In fact, the development and application of optical fiber sensors grew exponentially in the last decades as they demonstrate a huge versatility in different environments and the capacity of multiplexing several types of information in one device [14]. Nowadays, its usage is widely spread over automotive, food, and technology industries as it can be used as a humidity, strain, chemical, and biological sensor [14][15]. More recently, another technology has revolutionized the field of materials. Graphene has proven to be a super material in terms of its characteristics and applications. Indeed, after its synthesis in 2004, graphene rapidly became one of the most studied materials with a wide range of applications like photonics and electronics [16]. Graphene and other carbon allotropes also show electrochemical sensing features that can be implemented to detect aquaculture parameters [17][18].

1.2 Objectives

This work focuses on the development of highly sensitive fiber optic sensors with potential application for the detection and monitoring of crucial analytes present in aquaculture waters. The substances targeted in this work were ammonia and cortisol, which are of fundamental importance in maintaining optimal conditions for crops to develop healthily and efficiently.

For this purpose, a series of interferometers utilizing the Fabry-Pérot cavity principle were made using liquid polyimide as a base material. In some of them, gold nanoparticles

were introduced into the polyimide-based mixture to evaluate the impact of this addition on their sensitivities. Besides that, to create interferometers specifically responsive to ammonia, oxazine 170 perchlorate was mixed with the polyimide. All of them were subjected to strain, temperature, and refractive index evaluation to assess their sensibilities and later, in a novel approach, a CO_2 laser was employed to induce the formation of a LIG layer atop the interferometers cavity.

During this work stage, different laser parameters were used to assess the quality and penetration of LIG within the Fabry-Pérot cavity. Once the ideal laser parameters were determined, the interferometers underwent a further evaluation to assess any potential alterations in their sensitivities resulting from the introduction of the LIG coating. For that, the interferometers were again tested for the refractive index to evaluate whether there were any changes.

Finally, the interferometers were functionalized to make them cortisol sensitive and their performance was evaluated for sensitivity, selectivity, and pH responsiveness. Concerning ammonia, some interferometers with and without the LIG coating were used for the detection.

This work presents a novel lab-on-fiber approach for the detection of cortisol and ammonia using a functionalized LIG coating directly inscribed onto a Fabry-Pérot cavity. Furthermore, as is shown by the wheel graph from fig. 1.1, this work encompassed several areas of knowledge and therefore presents a complexity worthy of note.

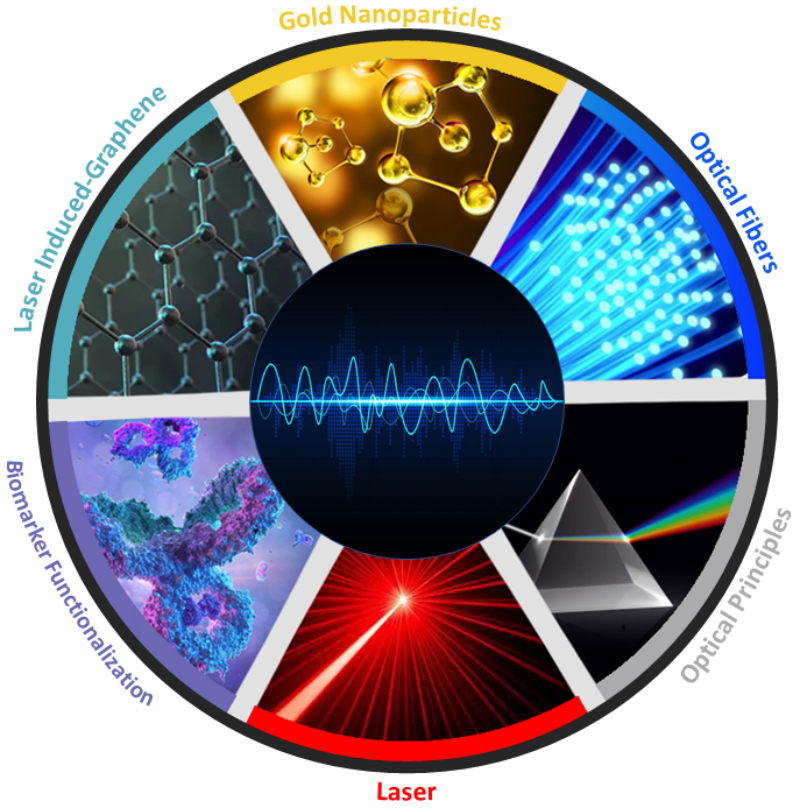

Figure 1.1: Wheel graph representing each field approached in this work.

— 2 —

Theoretical concepts and State of the art

The origin of light, as a word, is contemporary with the beginning of Mankind, with one of the most interesting roots coming from the prehistoric Germanic term *lingkhtaz*, meaning "something full of air and not heavy" as Jonh Ayto said [19]. In fact, this idea of something massless lasts to the present day, but the nature of light has shown a big mystery for the scientific community over time. On one hand, Isaac Newton describes the propagation of light as a rectilinear motion of crepuscular particles but, on the other hand, Christian Huygens explains reflection and refraction laws based on an undulatory theory, proved by Thomas Young and its double split experiment. Albert Einstein claps them together suggesting that light behaves as both wave and particle, known as the duality of light. To prove this convergence, one can begin by understanding in which situations these behaviors manifest themselves.

2.1 Opctical and Physical principles

James Maxwell, moved by undulatory theory, describes light as an electromagnetic wave and, therefore, a conjugation of vibrations between an electric and magnetic field. From his equations and assuming an undisturbed medium, the magnetic field, $\overrightarrow{H}$, the electric field, $\overrightarrow{E}$, and magnetic induction, $\overrightarrow{B}$, satisfy the following equation [20]:

$$\overrightarrow{B} = \mu_0 \overrightarrow{H} \tag{2.1}$$

$$\nabla^2 \overrightarrow{E} - \mu_0 \varepsilon_0 \frac{\partial^2}{\partial t^2} \overrightarrow{E} = 0 \tag{2.2}$$

$$\nabla^2 \overrightarrow{B} - \mu_0 \varepsilon_0 \frac{\partial^2}{\partial t^2} \overrightarrow{B} = 0 \tag{2.3}$$

where $\mu_0 = 4\pi \times 10^{-7}$ Hm^{-1} is the magnetic permeability and $\varepsilon_0 = \frac{10^{-9}}{36\pi}$ Fm^{-1} is the electric permittivity in vacuum. Both these differential equations correspond to the wave equation and so the propagation speed, v, is described by:

$$v = \frac{1}{\sqrt{\mu_0 \varepsilon_0}} = c = 2.998 \times 10^8 \text{m/s} \tag{2.4}$$

where c is the vacuum light speed calculated by Fizeau [21], which proves the undulatory nature of light. Furthermore, the electric permittivity and magnetic permeability are idiosyncratic of the propagation medium. This implied that the speed of light varies with the medium, and so, has been defined a ratio between vacuum speed and medium speed that describes the way that light's rays bend when they move between different mediums, known as the refractive index (RI), n [22] [20]:

$$n = \frac{c}{v} = \sqrt{\frac{\mu\varepsilon}{\mu_0 \varepsilon_0}} \tag{2.5}$$

where ε and μ are de medium's electric permittivity and magnetic permeability, respectively.

When an electromagnetic wave travels between two mediums with different refractive indices, n_1 and n_2, part is reflected and part is transmitted, as can be observed in fig. 2.1a. Assuming that wave propagation can be described geometrically as a linear motion, the angle between the incident ray, θ_i, and the normal to the plane separating the two mediums are equal to the angle between the refracted ray, θ_r, and the normal to that plane. This relation called reflection law is given by [22] [20]:

$$\theta_i = \theta_r \tag{2.6}$$

whereas, the relationship between the incident angle and the transmitted angle, θ_t, called Snell's law is given by:

$$n_1 \sin\theta_i = n_2 \sin\theta_t \tag{2.7}$$

For the above case, $n_1 < n_2$ and consequently $\theta_t < \theta_i$ although whenever $n_1 > n_2$ there is an angle of incidence such that the angle of transmission is $\pi/2$, fig. 2.1b. For incident angles greater than this, all light is reflected at the interface in a total internal reflection phenomenon. This angle is the critical angle, θ_c, and is described by [22] [20]:

$$\theta_c = \sin^{-1}(\frac{n_2}{n_1}) \tag{2.8}$$

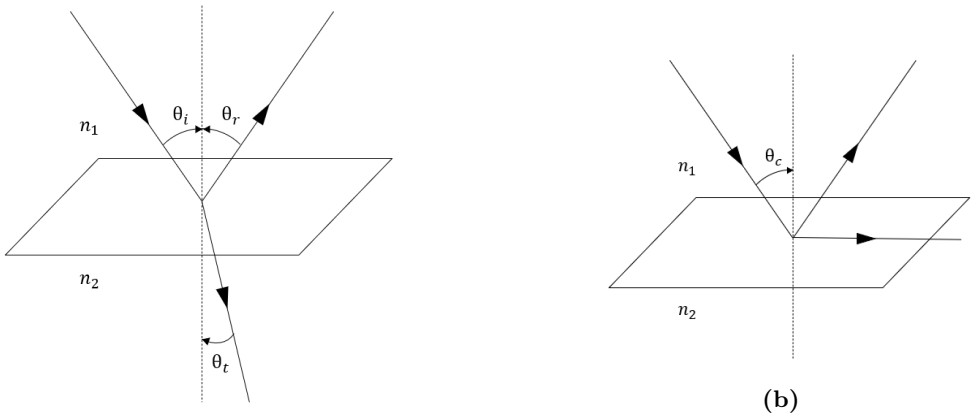

(a) **(b)**

Figure 2.1: Behaviour of light traveling between different propagation media.

Although wave theory correctly describes much of optical science, there are nevertheless some aspects that are not considered if the duality of light is not taken into account. For example, the photoelectric effect demonstrates that when the light hits a metal surface, electrons are emitted. The characteristics of the emitted electrons depend on the light wavelength, which implies that light is composed of particles. In his quantum theory, Einstein describes the energy of light as being carried by these particles, called photons. Its energy, E, is proportional to the electromagnetic frequency, ν, [23]:

$$E = h\nu \tag{2.9}$$

where $h = 6.63 \times 10^{-34}$ Js is the Plank's constant. As described by Einstein's theory of relativity, every particle shows momentum and photons are no exception. However, photons are massless particles and due to that, haven't static energy, mc^2. Photons's momentum, p, and velocity, v, are so defined by [23]:

$$p = \frac{\sqrt{E^2 - m^2c^4}}{c} = \frac{E}{c} \tag{2.10}$$

$$v = \frac{pc^2}{E} = c \tag{2.11}$$

From eq. 2.11 it is concluded that photons velocity is equal to vacuum light speed, c, which proves the corpuscular behavior and so the duality of light.

With the emergence of these discoveries, a new area of physics began to emerge and to develop new tools based on the fundamental principles of optics. Among them, the arrival of fiber optics opened the door to a whole new world of telecommunications and fiber optics-based sensors. Many optical sensors with small dimensions, with high sensitivities, highly resilient against electromagnetic interferences, and with better resolution were produced and showed greater versatility in the number of parameters measured when compared with traditional sensors [24].

2.1.1 Optical Fibers

Optical fibers are a waveguide that transmits light throughout their axis and is composed of a core, a cladding, and a coating, as represented in fig. 2.2a. To transmit light for long distances, optical fibers use the principle of Total Internal Reflection (TIR) in order to minimize losses to the cladding. To achieve it, the RI of the core, n_{Core}, needs to be greater than the cladding's RI, $n_{Claddling}$. For this purpose, the fibers are produced in such a way as to obtain a step-index, like that represented in fig. 2.2b. The coating layer, for instance, serves both to protect and strengthen the fiber and for the purpose of functionalization.

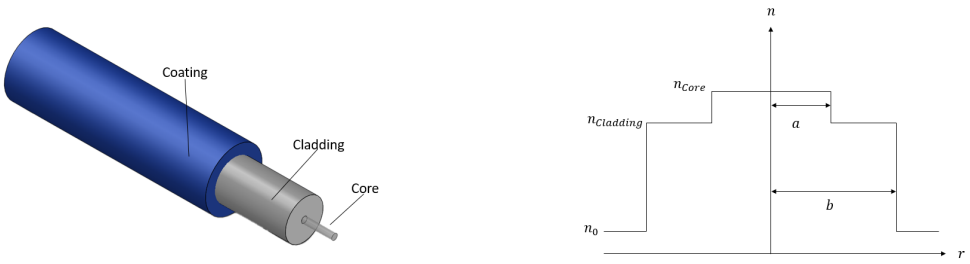

(a) **(b)**

Figure 2.2: (a) Schematic representation of a fibre and its constituents; (b) Representation of the step-index.

Furthermore, considering fig. 2.3, when ray 1 goes into the fiber's core undergoes a deviation such that:

$$n_0 \sin\theta_i = n_{Core} \sin\theta_t \tag{2.12}$$

where n_0 is the RI of the propagation medium of light before entering the fiber. If the angle ϕ is greater than the critical angle given by eq. 2.8 ($\sin\theta_{max} = \frac{n_{Cladding}}{n_{Core}}$), then the ray suffers TIR. So, there is a maximum angle, θ_{max}, below which every ray is confined on the fiber's core. Otherwise, some intensity is transmitted to the cladding like ray 2. So θ_{max} can be define as function of n_{Core} and $n_{Cladding}$ [25]:

$$n_0 \sin\theta_{max} = (n^2_{Core} - n^2_{Cladding})^{\frac{1}{2}} \tag{2.13}$$

The result of eq. 2.13 defines the cone formed by the rays guided by the fiber and is defined as fiber's Numerical Aperture (NA):

$$NA = (n^2_{Core} - n^2_{Cladding})^{\frac{1}{2}} \tag{2.14}$$

The number of modes that can propagate over the fiber depends on the diameter of the core, a_{core}, on NA, and on vacuum wavelength, λ_c, as it is described by the following equation [26]:

$$V = \frac{2\pi a_{\text{core}}}{\lambda_c}(n^2_{Core} - n^2_{Cladding})^{\frac{1}{2}} = \frac{2\pi a_{\text{core}}}{\lambda_c} NA \tag{2.15}$$

This is especially important to characterize an optical fiber, as it can be defined as Single-Mode Fiber (SMF) if V takes values under 2.405 or Multi-Mode Fiber (MMF) if V takes values above that number. Their major differences are related to the greater distance that SMF can propagate light with low attenuation when compared with MMF. However, once MMF can propagate several modes, it can also transmit more information than SMF. For this reason, SMF and MMF have different applications.

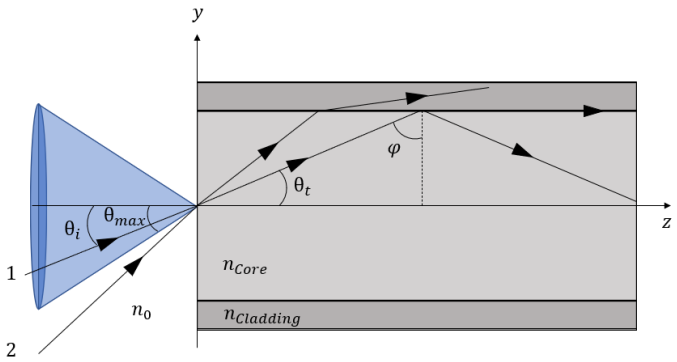

Figure 2.3: Representation of the cone of acceptance formed by the incoming light rays.

The implementation of fiber optics in the telecommunication industry revolutionized it. The rate at which information is delivered has accelerated rapidly, such as its quality, capacity, and distance over which it can be transmitted. But the waveguide capability is only one of the advantages of fiber optics, several sensors, lasers, and signal amplifiers have been developed in the fiber itself based on the concept of multiplexing information [27].

2.1.2 Fabry-Pérot interferometer (FPI)

Interferometers based on Fabry-Pérot's cavity using optical fibers are just one of these applications. When an incident ray travels through a thin film, as the one represented in fig. 2.4, part of the light may suffer multiple reflections and another part is transmitted as a result of the reflectivity of the film's surfaces. The transmitted light interferes and generates a spectrum of destructive and constructive interference that depends on the film's thickness, L, the RI of the film's material, n_{Cavity}, and, transmission angle, θ_t.

In this work, this principle is applied to optical fibers. In this case, one section of the fiber is replaced with another material (air, polyimide, etc...), and the interface between fibers and the material makes the reflective surfaces needed to achieve multiple reflections. In fig. 2.5 is represented the apparatus where the light hits the interface with an angle θ_t null, then the dip wavelengths are described by [28]:

$$\lambda_m = \frac{4n_{\text{Cavity}}L}{2m+1}(m = 1, 2, 3, ...) \tag{2.16}$$

Also, the distance between the adjacent dips or the so-called Free Spectral Range (FSR) can be described by the following equation [28]:

$$FSR = \frac{\lambda^2}{2nL} \tag{2.17}$$

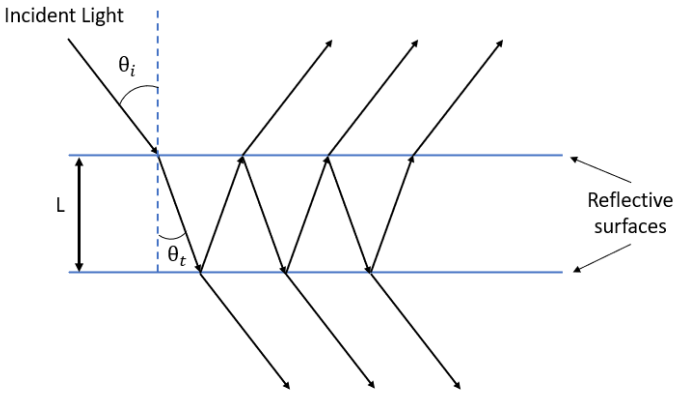

Figure 2.4: Representation of the multiple reflections that underlie the Fabry-Pérot cavity phenomenon.

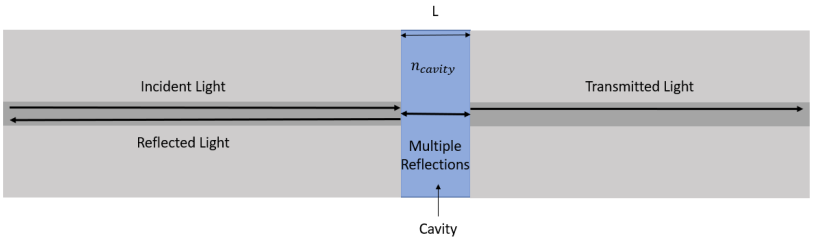

Figure 2.5: In fiber approach to realize an interferometer based on the Fabry-Pérot cavity.

From eq. 2.17 it is easily derived how the wavelength can vary:

$$\Delta\lambda = \frac{\partial\lambda}{\partial n}\Delta n + \frac{\partial\lambda}{\partial L}\Delta L = \lambda(\frac{\Delta n}{n} + \frac{\Delta L}{L}) \tag{2.18}$$

As eq. 2.18 shows, the shift in wavelength depends on the variation of cavity's RI and, L, and so the interferometer spectrum may suffer deviations depending on external factors such as temperature, pressure, or humidity variations that affect these parameters. In fact, the cavity length, L, is obviously affected by strain forces but temperature can also make the cavity expand or compress changing its length [29]. It is reported sensibilities range between 0.6 pm/°C to 5.2 nm°C for temperature sensing applications [29][30][31][32][33], and sensibilities range between 2.3 pm/$\mu\varepsilon$ to 13.9 pm/$\mu\varepsilon$ for strain sensors [29][32][31]. Some FPI can also sense changes in relative humidity, it can absorb some moisture changing the cavity RI, as was reported in [34] with a sensibility of 70 pm/%R or in [35] with a sensibility of 280 pm/%R. But much more sensing applications can be made using FPI, mechanical vibration sensing, acoustic wave sensing, ultrasound sensing, voltage sensing, magnetic field sensing, pressure sensing, flow velocity sensing, gas sensing, liquid level sensing, and RI sensing are some other application referred in [36]. These reports show that FPI are good for a variety of sensing applications, however, there are also ways to improve the performance of these sensors. Specifically, through the Vernier effect.[37][38].

2.1.3 Vernier Effect

A sensor based on this effect reported in [28] shows an increase in the sensibility of 14.2 times from 0.5361 nm/%R to -7.6221 nm/%R. Moreover, in [39] is reported a sensibility increase of 2000 times from 1.4 pm/°C to 33.06 nm/°C. These enhancements allow the fabrication of highly sensitive sensors for a wide range of applications.

The VE was initially used in length measurements, in devices like the caliper or the micrometer where a sliding scale slides on a reference one. The scales are graded differently but periodically they overlap and this effect is used to increase the measurement resolution and precision [37][38]. For optical purposes, two FPI with different FSR can be used as the sliding and the reference scales to enhance the sensitivity. As fig. 2.6 shows, the VE can be achieved by placing the two FPI in a parallel or in a series configuration, both the spectrums interfere with each other resulting in a series of fringes modulated by a Vernier envelope. In addition to the use of FPI, other optical interferometers are used to achieve the Vernier effect, such as Mach-Zender Interferometers (MZI), Michelson Interferometers (MI), Sagnac Interferometers (SI), or a combination of these [38][37].

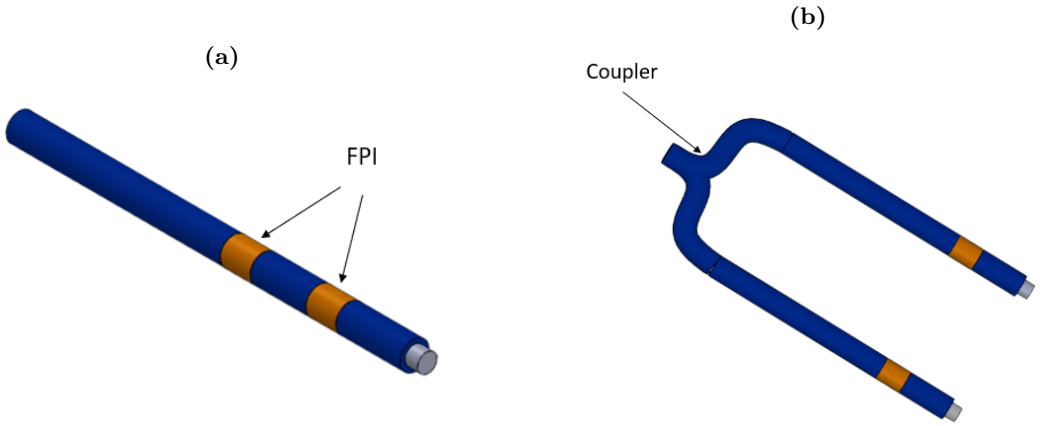

Figure 2.6: Schematic representation of the possible configuration for VE: (a) in series and (b) in parallel.

In most cases where the Vernier effect is applied, the reference FPI is used in a static configuration, i.e. it is kept at equal conditions during the entire sensing period, while the sensing FPI is used as a sensor. In this case, the FPI reference, FP_R, spectrum doesn't change, and, the sensing FPI, FP_S, spectrum experiences a shift in wavelength, $\Delta\lambda_{FPS}$, the VE spectrum also shifts by $\Delta\lambda_{VE}$, as it is shown in fig. 2.7a [37][38]. This configuration is called the traditional Vernier effect [40][41]. However, other two phenomenons can occur when the FP_R is submitted to environmental variations as well: a) Vernier Effect Reduced - When $\Delta\lambda_{FPR}$ and $\Delta\lambda_{FPS}$ are both positive or both negative, the VE sensibility increase is lower compared to traditional VE, like it is shown in fig. 2.7b [40][41]; b) Vernier Effect Enhanced - In another hand, when $\Delta\lambda_{FPR}$ and $\Delta\lambda_{FPS}$ has opposite signs, the VE sensibility increase is higher compared to VE traditional and to the VE reduced, as fig. 2.7b shows [40][41].

Taking into account the parallel configuration, the eq. 2.16, and eq. 2.17, FP_R and FP_S are described by:

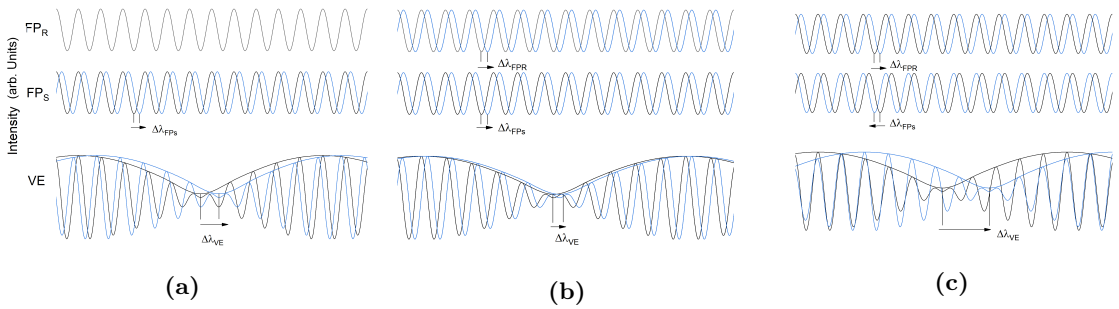

Figure 2.7: Representation of the three different types of Vernier effect: (a) Traditional VE, (b) Reduced VE, and, (c) Enhanced VE.

$$FSR_{\mathrm{FP}_R} = \frac{\lambda^2}{2n_R L_R} \tag{2.19}$$

$$FSR_{\mathrm{FP}_S} = \frac{\lambda^2}{2n_S L_S} \tag{2.20}$$

where n_R, L_R are the RI and cavity length of FP_R and n_S, L_S are the RI and cavity length of FP_S. Then the FSR of the envelope can be defined by [40]:

$$FSR_{\mathrm{envelope}} = \frac{FSR_{\mathrm{FP}_R} FSR_{\mathrm{FP}_S}}{|FSR_{\mathrm{FP}_R} - FSR_{\mathrm{FP}_S}|} \tag{2.21}$$

From eq. 2.21 it is concluded that the smaller the difference between the FSR, the greater is FSR_{envelope}, however, its visualization ends up being conditioned by the wavelength range covered by the equipment used to acquire the reflection spectra. Another parameter used to characterize the Vernier effect is the magnification factor, M, which compares the amplification related to each interferometer, M is then defined by [40][38][37]:

$$M_{\mathrm{FP}_R} = \frac{FSR_{\mathrm{FP}_S}}{FSR_{\mathrm{FP}_R} - FSR_{\mathrm{FP}_S}} = \frac{S_{\mathrm{envelope}}}{S_R} \tag{2.22}$$

$$M_{\mathrm{FP}_S} = \frac{FSR_{\mathrm{FP}_R}}{FSR_{\mathrm{FP}_R} - FSR_{\mathrm{FP}_S}} = \frac{S_{\mathrm{envelope}}}{S_S} \tag{2.23}$$

where S_{envelope}, S_R, S_S are the Vernier envelope, reference FPI and sensing FPI sensibilities, respectively. From eq. 2.22 and eq. 2.23, it follows that the M factor increase with the decrease of the difference between the interferometers FSR. On the other hand, higher M values result in higher Vernier sensibilities. Although it is feasible to achieve high sensibilities, there are some problems related to this. As discussed above, the equipment used for data acquisition may be limiting when the wavelength shift is greater than the range covered. Besides that, to achieve such high sensibilities it is necessary that the FSR of the interferometers are as close as possible. According to eq. 2.17, the lengths of the cavities can be adjusted for this purpose. However, it is experimentally difficult to obtain such small differences [38]. It is therefore necessary to strike a balance between the limitations of the available equipment and the desire for ultrasensitive sensors.

Besides the relatively recent development of fiber optic sensors, another material has also emerged with desirable properties for the same application. Since its discovery, graphene and its derivatives have been useful in the development of increasingly versatile and dynamic sensors.

2.2 Laser Induced Graphene (LIG)

Graphene is a two-dimensional transparent material with two atoms per unit cell as a result of its hexagonal honeycomb structure, where each carbon atom bonds to three others by covalent bonds. This characteristic forces the s orbital and two of the three p orbitals to hybridize and form three sp^2 orbitals. While the electrons of the sp^2 orbitals bond to each other forming σ bonds, the electrons of the p orbitals, which have not hybridized, bond to each other forming π bonds that are delocalized over the sheet, as is shown in fig. 2.8a. Once carbon atoms are indeed surface atoms, graphene is highly sensitive to its surrounding environment making it suitable for sensing applications. Furthermore, graphene as a single layer shows three acoustic and three optical branches as a result of phonon dispersion [42]. Fig. 2.8b represents the electronic (gray hexagons) and first phonon (red line) Brillouin zones in addition to the Dirac cones due to electronic dispersion. Near K and K' points and below 1 eV the energy dispersion is described in such a way that forms these Dirac cones [43]. This linear dispersion enables the electrons to behave in a manner similar to light. Besides that, graphene has a low scattering rate and the conduction is near to ballistic [44]. Another great feature presented by graphene is its mechanical strength making it one of the strongest materials, it was already reported that graphene can present a modulus young up to 1.1 TPa [45].

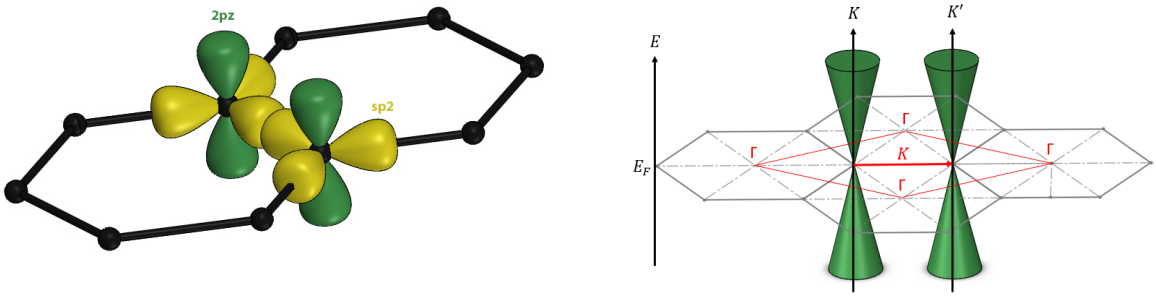

(a) **(b)**

Figure 2.8: (a) Atomic structure of graphene and representation of the electronic cloud of the carbon atoms. (b) Brillouin zone of graphene and representation of the electron dispersion in the form of Dirac cones.

Since the first successful graphene preparation by micromechanical exfoliation method [46], other preparation technics were developed: chemical exfoliation method [47], reduction of graphene oxide method [48], epitaxial growth method [49], chemical vapor deposition (CVD) method [50], and laser-induced graphene (LIG) [51]. Many of these preparation methods produce high-quality graphene, however, some need an ultra-high vacuum and high-temperature conditions, others use solvents or reduction steps that change the graphene's

features making it unsuitable for sensing applications, and others aren't appropriate for producing large quantities of graphene. However, LIG, despite its foamy and porous texture and multi-layer graphene outcome, maintains the desirable conductivity and mechanical properties that make it suitable for sensing proposes. Furthermore, special environmental conditions, supplementary solvents, or reduction steps aren't needed, making it an easier, cheaper, and simple process [51] [52].

In the LIG method, a laser beam is focused on a substrate like a PI sheet, a polymer composed of hydrogen, carbon, nitrogen, and oxygen. The laser beam heats up the PI and produces LIG and gaseous molecules like CO, H_2, and hydrocarbons ($C_xH_yN_z$) [52]. This process involves two steps: carbonization and graphitization. The first one, and considering a CO_2 laser, occurs at 673 K and produces an amorphous tetrahedral carbon arrangement in which carbon atoms bond with each other by sp^3 bonds. At 773 K, the gaseous substances are released, sp^3 bonds are broken and sp^2 bonds are formed and the amorphous arrangement crystalizes forming LIG [53]. The foamy and porous texture can be explained by this gaseous release process. The formation of LIG is basically the same regardless of the type of substrate. However, the interaction laser-subtract is different for different types of laser and some processes are more prevalent than others: photothermal process (laser with a wavelength larger than 400 nm) or photochemical process (laser with a wavelength smaller than 400 nm) [52]. Indeed, for low-wavelength lasers, the photon energy is enough to break the chemical bonds between atoms and generate LIG without much vapor releasing, as happens with longer wavelength lasers, making the LIG less porous. Besides that, laser parameters play an important role in LIG features. Different applied powers or different laser speeds change the way that rearrangement and gaseous release occurs affecting resistance, conductivity, thickness, and crystallite sizes, for example, [54].

Graphene and fiber optic sensors are two of the fastest-growing fields in recent decades, much of this progress is due to the evolution of society into an age where the power of information is valued as never before. As Kofi Annan said "Knowledge is power. Information is liberating. Education is the premise of progress, in every society, in every family", this principle is so ingrained in the way we live that it is unthinkable to imagine a future without the constant flood of information we are subjected to.

2.3 Sensors

Sensors as a whole are a vital part of this development, as they are the eyes and ears where Mankind can neither see nor hear. As they enabled the first trips to the moon, the discovery of the Higgs boson, and the first images of black holes, among others.

Sensors are devices that can detect a stimulus, whether physical, chemical, or biological, among others. Usually, they consist of a sensing and a transducer element, the last converts the stimulus into an electrical or optical signal. The important characteristics that a sensor relies on are its linearity, sensitivity, repeatability, selectivity, stability, and resolution. Optical and electrical are the main types of sensors, where the first is more versatile, with a more fast response, can multiplex multiple types of information, and is immune to electromagnetic

noise. In fact, Fiber Optic Sensor (FOS)s are preferred because of all these characteristics over their electrical counterparts.

There are several principles used by FOSs for the detection of any kind of physical, chemical, or biological property. Besides the interference principle used by the FPI, MZI, MI, SI as discussed above, here are some other principles used in FOS:

- **Intensity** - The light propagation through the fiber can be affected by physical or chemical external variations. This can attenuate the light intensity and be used as a sensing mechanism [55].
- **Fiber Bragg Grating (FBG)** - It is possible to periodically modify the refractive index of the fiber core, creating a phase grating. This grating works as a reflector for a specific wavelength, the Bragg's wavelength. And, so the FBG-based sensors monitor the variations of the Bragg peak in response to external stimulus [56]. One variation from traditional FBGs is the Tilted Fiber Bragg Grating (TFBG)s, these gratings result from the inscription of the grid tilted by an angle θ_{TFBG} in relation to the propagation axis. Because of that, not only the forward and counter-propagation core modes are coupled, as it happens in a FBG, but also the coupling between core and cladding modes may occur [57]
- **Evanescent Wave** - The evanescent wave is a wave created when light, in an angle greater than the critical angle, travels between mediums with different RI. The majority of the light energy is totally internally reflected but some of them pass to the second medium, forming an evanescent wave that decays rapidly. In an optical fiber, light always travels with the characteristics described above, so the evanescent wave phenomenon is used at the boundary between the fiber and the surrounding medium. The variation of the evanescent wave spectral response due to variations in the surrounding medium can be used as a sensing mechanism [58].
- **Polarimetric sensors** - In this type of sensor light polarization is used to detect the external stimulus. The light is emitted with a known polarization that can be altered due to the interaction with the medium, making it suitable for sensing applications [59].
- **Surface Plasmon Resonance (SPR) based sensors** - The SPR effects occur when the light traveling through a dielectric material hits a metallic surface and originates a collective oscillation of free electrons (surface plasmons) at the interface. For certain wavelengths, their electric field couples with the surface plasmon leading to a resonance condition that causes a huge decrease in the reflection at this resonance wavelength. Using optical fibers coated with gold (Au) or silver (Ag), the same effect can be achieved. As SPR is very sensitive to changes in refractive index at the metallic surface, it can be used to detect chemical reaction that occur there [60].

In this work, is proposed the development of sensors with the potential for the detection of analytes of interest in aquaculture waters. Many of these substances are biological components such as proteins, hormones, toxins, Deoxyribonucleic Acid (DNA), and other biomolecules. For that reason, the transducer layer is often composed of enzymes or antibodies that have an

affinity for these analytes. Taking into account the characteristics of these sensors, they are often called biosensors.

2.3.1 Biosensors: Cortisol and Ammonia

The importance of cortisol and ammonia detection has already been discussed and now it is key to understand what has been done so far on this topic.

Most FOSs developed for cortisol detection use the SPR effect for this purpose. As SPR is very sensitive to RI variations, the functionalization of the metal surface to cortisol allows the chemical reactions between the analyte and its antibody to take place at the metal surface and to be easily detected due to the local variation of refractive index. In [61], a TFBG coated with Au was functionalized to cortisol using a mixture of anti-body, N-hydroxysuccinimide (NHS) and ethylcarboiimide hydrochlorine (EDC) prepared in phosphate-buffered saline (PBS). The lower envelope local maximum was followed obtaining a sensitivity of 0.275 ± 0.028 nm/ng.mL^{-1} and linearity until 10 ng/mL. In other work, a D-shaped optical fiber was also coated with gold and functionalized obtaining a sensibility of 0.65±0.02 nm/log(ng/mL) between 0.01 and 100 ng/mL [62].

Regarding sensors dedicated to ammonia were reported at [63] a FPI where the cavity was filled with a mixture of a curable resin and oxazine 170 perchlorate, as oxazine reacts with the dissolved ammonia, the cavity RI changes and a wavelength shift occur. The sensibility obtain was as high as 4.3 nm/ppm. Besides that, in another article, a metallic layer was deposited at the end of a polymeric optical fiber coated with oxazine, working as a mirror and enabling sensor usage in reflection mode. The sensor proposed was capable of sensing ammonia at concentrations as low as 100 ppb [10]. Oxazine was also used in [64] by dip-coating a plastic optical fiber in it, creating an oxazine layer sensitive to ammonia. This sensor has a detection limit of 1.4 ppm with under 10 seconds response time.

The high specific area of LIG's surface is an interesting characteristic. It allows an easier electron transfer between LIG and any analyte of interest. In this way, it can be used as a transducer for electrochemical sensors. In fact, this sensing application for LIG is widely reported, glucose [65], dopamine [66][67], ascorbic and uric acid [67] are some of the interest analytes which can be detected by electrochemical sensors using LIG. It is reported as well, a very interesting nitrate and ammonium sensor [68]. This study proposes to develop a solid-contact ion-selective electrode (SC-ISE) based on LIG produced on a PI sheet substrate using an Ultra-Violet (UV) laser. For ion selectivity, was used a mixture of methyl triphenylphosphonium bromide and nitrocellulose dissolved in a solution of 2-propanol, 2-nitrophenyl octyl ether, PVC, tetrahydrofuran, and tri-dodecyl methylammonium nitrate to functionalize the LIG electrode to be sensitive to nitrate. This electrochemical sensor showed a sensitivity of -54.8 ± 2.5 mV/dec and a detection limit of 20.6 ± 14.8 μ M on dionized water (DI water). Furthermore, the sensor was also tested in a complex environment (soil matrix) and showed a similar performance when compared with commercial nitrate sensors. Besides that, in [69] an electrochemical sensor based on Gold Nanoparticles (AuNPs) and Graphene Oxide (GO) was proposed for cortisol detection. It showed a limit detection of 10^{-18}

mol/L and an operating range of between 0.5 × 10^{14} and 10^{-18} mol/L. Another AuNPs/GO electrochemical sensor was developed with a –8.2443 log ((Cortisol concentration)ng/mL) sensibility for a 0.1– 1000 ng/mL range [70]. This LIG's electrochemical features can be used in conjunction with the optical sensors shown above, for sensing proposes.

2.3.2 LIG and Optical fibers

A way to combine these different fields is described in [56]. Using a PI coated fiber was possible to create a LIG layer around a TFBG structure, obtaining a sensibility enhancement of almost 1.5 times when compared with sensors without the LIG coating. In another work, [71] used a hollow-core fiber dipped coated in PI to make a LIG layer that has produced an ultrawide humidity sensor capable of measuring the air moister between 5 and 95 %RH with 0.187 dB/% RH sensibility. Most interesting was the work developed in [18], where an electrochemical sensor for dopamine arrest was developed in a LIG layer created around an optical fiber. It showed a sensitivity of 5.0 μA μM^{-1} cm^{-2} and high selectivity to dopamine. These novel sensors are very promising and open a path to the development of hybrid sensors using the optical characteristics of the fiber and the electrochemical characteristics of the LIG. This approach is a recent advance with few dedicated papers, being an emerging technology, especially due to the work presented in [56] and [18]. In both works a continuous CO2 laser was used to produce LIG on the fiber surface. Fig. 2.9 shows the SEM images from [56] and [18] work, as is possible to notice the LIG formed is porous and presents some homogeneity, however, some substructures are observed as well. Furthermore, the cross-section image of one of the fibers shows that all the polyimide has been transformed into LIG. These results present a solid base for the creation of LIG in fibers coated with polyimide necessary for the development of this work.

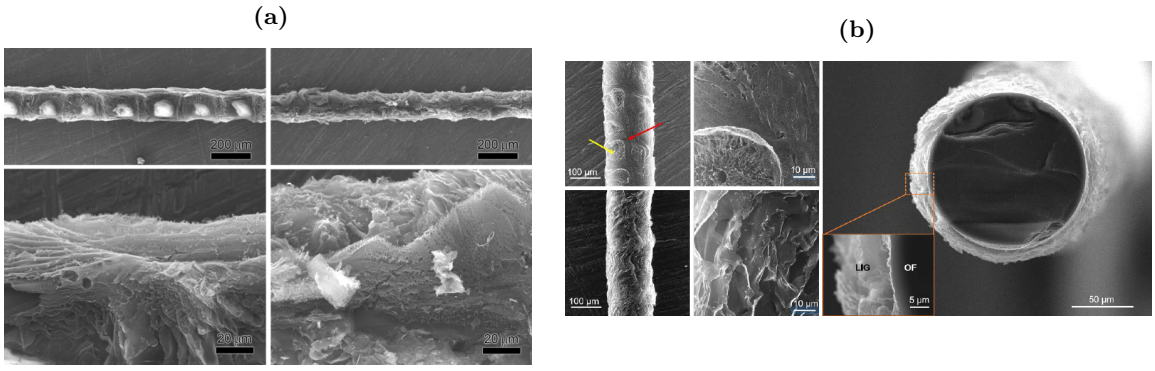

Figure 2.9: Longitudinal and cross-section SEM images of LIG coated fibers from (a) [56] and (b) [18].

— 3 —

Experimental and Characterization

3.1 Experimental procedure

In the following sections are described all the experimental activities carried out to develop the proposed sensors.

3.1.1 Interferometer fabrication

In this work, two SMF (Corning SMF-28e(125/8.2)) were cleaved and placed on a three-dimensional positioner, like the one shown in fig. 3.1. One of them was also connected to an interrogator (Luna HYPERION si255) to monitor its reflection spectrum. Using the displacement screws and a stereomicroscope (Leica A60), the two SMF were aligned in order to maximize the intensity of the fringes observed in the reflection spectrum (ENLIGHT Sensing Analysis Software was used for all spectrum acquirements). Furthermore, a small gap was left to be filled with liquid PI (Sigma-Aldrich, 5g) as represented in the scheme presented in fig. 3.1. Note that with the current manufacturing process it is difficult to quantitatively control the length of the cavity. After that, this montage was placed in the thermal chamber (Climate Chamber 64L -70°C to 180°C WEISS TECHNIK, Model L C×64/70/3) to cure the polyimide with the heat treatment beginning at 40 ºC with an increment of 5ºC/min until 170 ºC. This temperature was maintained for 20 minutes, then cooled down slowly to ambient temperature. In table 3.1 are represented the cavity length (Gap) and the material that was used to make it, as it can be noticed some of the FPI were made with a slightly different process. Before the curing step, was mixed AuNPs and Oxazine in the PI glue. Further, in 3.1.3 and 3.1.5 will be described the amount of AuNPs and oxazine mixed with PI.

Table 3.1: Gap length and gap material of the different fabricated FPI.

	FP1	**FP2**	**FP3**	**FP4**	**FP5**	**FP6**	**FP7**	**FP8**	**FP9**	**FP10**
Gap(μm)	105	125	182	175	218	172	182	195	157	231
Gap Material	PI	PI AuNPs	PI AuNPs	PI AuNPs	PI	PI	PI Oxazine	PI Oxazine	PI	PI

.

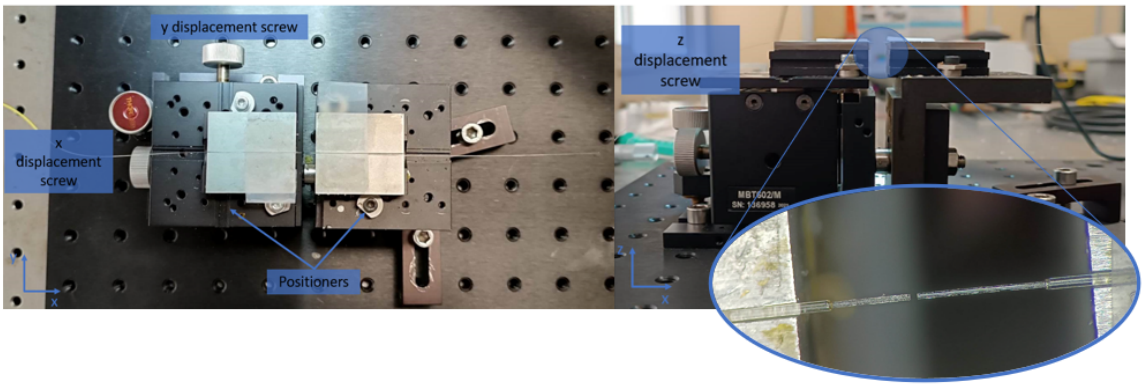

(a)

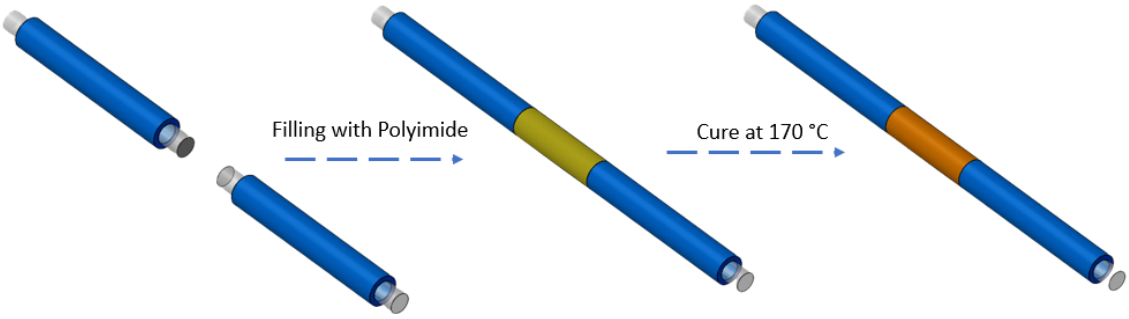

(b)

Figure 3.1: (a) Photography of the experimental setup for interferometer fabrication.(b) Schematic representation of the gap filling and the curing process.

3.1.2 LIG inscription

After the fabrication, the interferometer was subjected to a laser irradiation in order to transform the surface polyimide into LIG. The laser beam was passed along the fiber's axis to produce LIG, then the fiber was rotated 90°, and again the laser was passed along. The same procedure was made by rotating the fiber 180° and 270° in relation to the original position. This produces a uniform LIG layer around the interferometer as represented in fig. 3.2. The laser used was CMARK PRO 3 from Portlaser (CO_2 pulsed laser with a wavelength of 10.6 μm) and the control software is PTLMark - CO2 developed by Portlaser. The power output of the laser used is expressed in percentage of the maximum power that the system can reach. For this reason, was necessary to measure the power in watts for different power percentage outputs. The results are presented in fig. 3.2b.

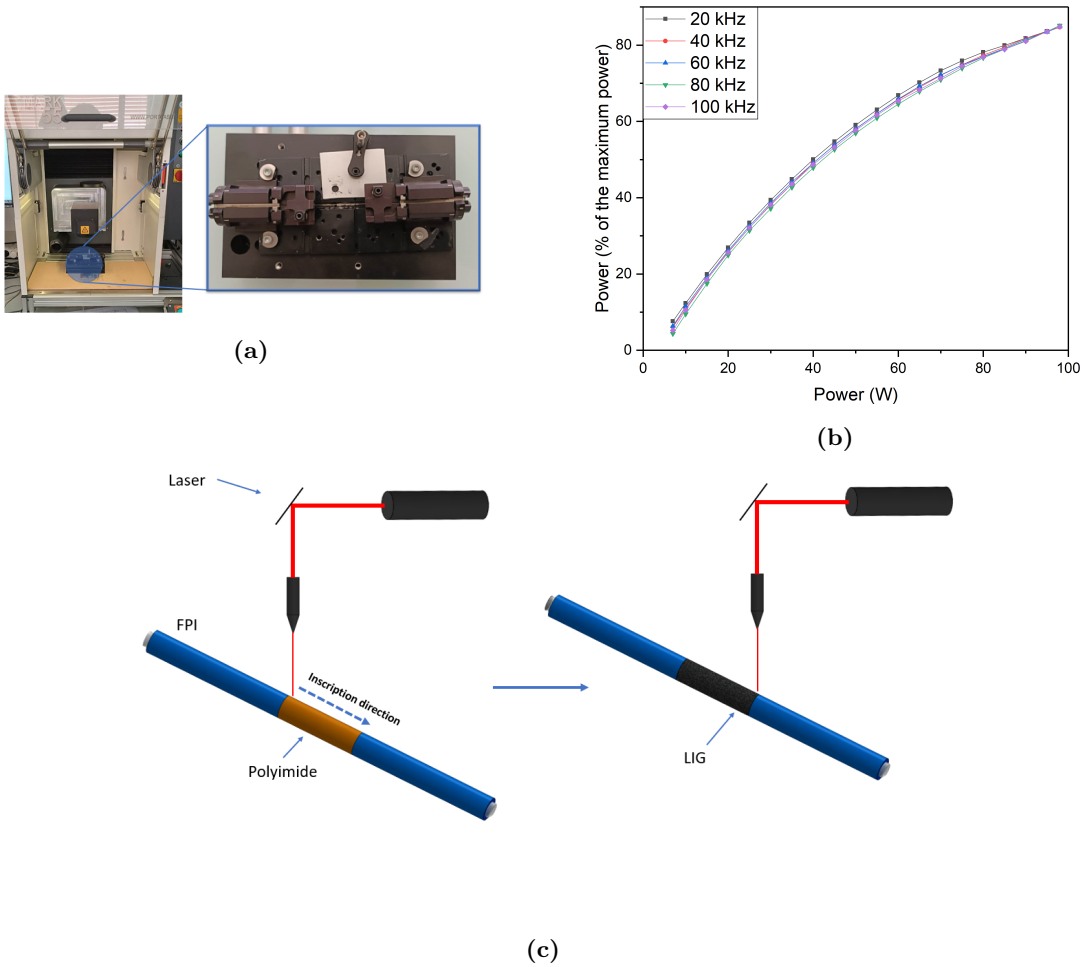

Figure 3.2: (a) Photography of the experimental setup where the fiber is placed into the holder and put under the laser.(b) Laser's output power percentage vs power measured in watts for 20, 40, 60, 80, and 100 kHz of pulse frequency, maintaining the pulse width constant. (c) Schematic representation of LIG fabrication process.

3.1.3 Gold Nanoparticles Synthesis process

The use of AuNPs was required in this work at two distinct stages: for mixing with the PI glue and for the fiber functionalization step.

The AuNPs were synthesized following the Turkevich protocol. This method uses gold salts dissolved in a solvent, like water. The solution is heated until a boiling temperature and a reduction agent is added to reduce gold ions (Au^{3+}) to gold atoms (Au^{0}). As the ions are reduced, the atoms begin to nucleate and form nanoparticles, the size can be controlled by adjusting the concentration of the salts, the reduction agent, or the reactions condition such as temperature or stir frequency. Usually, an stabilizing agent is used to prevent the aggregation of the AuNPs [72].

For this work, firstly a flask was washed with an aqua-regia solution (HNO_3 (Sigma-Aldrich, 65%-67%):HCl (Sigma-Aldrich, 37%)=1:3) and a $HAuCl_4$ solution (150 μl, 100 mM $HAuCl_4$ in 14.85 mL DI water) was laid on it. The solution was heated to its boiling temperature and then 1.8 mL of 38.8 mM sodium citrate solution (Sigma-Aldrich, 99.0%)) was added. The

final solution was heated to 110 °C for 5 minutes and then stirred for 10 more minutes. In the end, the AuNPs were analyzed by UV-Vis spectrometer and showed a peak at 519 nm that corresponds to an average size of 15 nm for the nanoparticles [58].

3.1.4 AuNPs coating and Cortisol functionalization

To coat the interferometers, it is important to first clean their surface of any impurities. Normally, is used a Piranha solution (with a volume ratio of 3:1 of H_2SO_4:H_2O_2) to clean and hydrolyze the fibers surface [58][73], however, the Piranha solution can be too aggressive to the LIG layer, for that reason in this first step was used ethanol to prepare the fiber surface. The interferometer was immersed in ethanol (Supelco, $\geq$ 99.9%) for 20 min and then it was dipped in a 1% ethanolic solution of (3-Mercaptopropyl)trimethoxysilane (MPTMS) (Sigma-Aldrich, 95%) for 2 hours at 40 °C. The MPTMS solution acts as an adherence facilitator for the AuNPs. Finally, the interferometer was immersed into the AuNPs solution for 12 hours [58][73].

For cortisol functionalization, the previously prepared fibers with AuNPs were submerged in 0.5 mM 11-Mercaptoundecanoic acid (MUA) (Sigma-Aldrich, 95%) for 5 hours, this step creates a layer of alkane chains and carboxyl (-COOH) groups above the AuNPs layer. The MUA contains a thiol (-SH) group that forms strong bonds with the AuNPs, besides that, gives stability for the functional molecules. A bath of EDC/NHS solution for 30 minutes was needed to attach the cortisol antibody. The solution contains 200 mM of EDC (Merck, 0.2 M) and 50 mM of NHS (Merk, 0.5M, 98%), this active the MUA's carboxyl groups making them more susceptible to bond with the antibody, and also ensures stronger bonds with the functional groups and more stability. Finally, the interferometer was ready to be dipped in a 500 μg/ml solution of anti-cortisol (Bio-Rad) [58]. After 24 hours, the interferometers were removed and the functionalization process ended. The cortisol functionalization process is represented in fig. 3.3

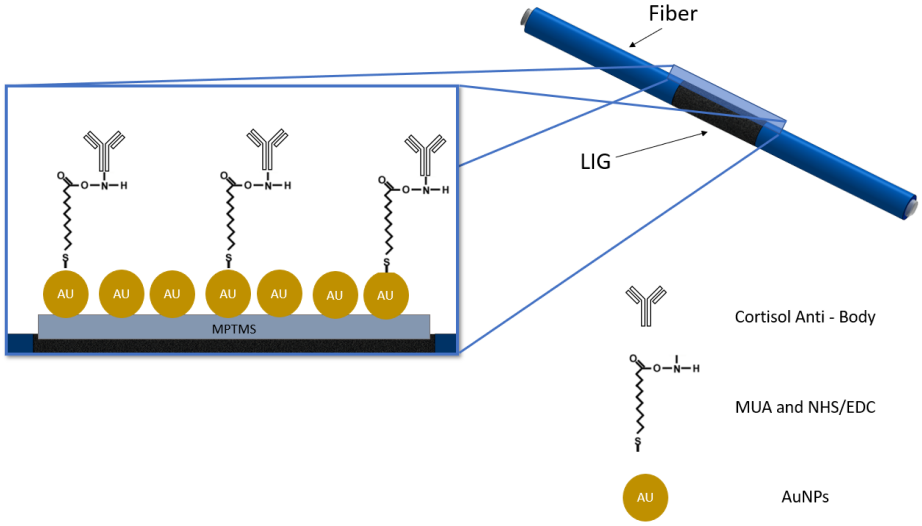

Figure 3.3: Schematic representation of the cortisol functionalization.

3.1.5 Ammonia functionalization

For ammonia detection, a new approach was implemented by simply mixing 1 mg of oxazine 170 perchlorate dye (Sigma-Aldrich, 95%) with 1 ml of PI glue. Due to the high viscosity of the PI glue, the mix was put into the centrifuge for 10 minutes to evenly blend the dye into PI glue. In the process, the color has changed from a yellowish-orange hue to a dark blue hue, as is possible to see in fig. 3.4 photographs.

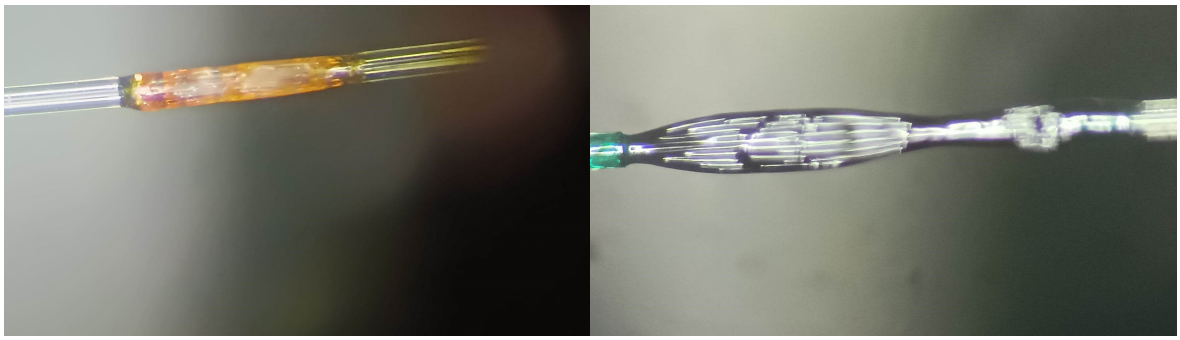

(a) **(b)**

Figure 3.4: Microspopic photography of a FPI made with (a) polyimide and (b) oxazine mixed with polyimide.

3.2 Characterization Techniques

To characterize structurally, morphologically, and investigate the optical characteristics of the sensors, several techniques were used such as SEM, Raman spectroscopy, and Attenuated Total Reflectance Fourier-Transform Infrared Spectroscopy (ATR-FTIR).

3.2.1 Scanning electron microscopy (SEM) and Energy Dispersive X-Ray (EDS)

Scanning electron microscopy (SEM) is a technique that enables a detailed analysis of the morphology and composition of the sample's surface. The main advantage over traditional optical microscopy is the limit of resolution. While optical microscopy uses photons with a wavelength on the visible spectrum as a source, which has a resolution limit of 200 nm, SEM uses an electron beam. This gives a better resolution once the highly accelerated electrons reach a few nanometres resolution [74].

Is important to understand what happens when electrons interact with the sample once signal acquisition depends on these interactions. There are two major types: in elastic scattering, the incident electron suffers a deflection as a result of the collision with the specimen nucleus or with the outer shell electrons with suchlike energy. Little or no energy is lost and the deflection angle is widely open, if this angle is greater than 90° the scattered electron is called a backscattered electron (Backscattered Electron (BSE)) and gives very important information to build the image. BSEs are constantly deflected by the sample's nucleus so they travel within the sample and emerge far from the beam spot. Because of that, BSEs give information about the composition and features beneath the surface; in inelastic scattering, the interaction between beam electrons and sample atoms causes a transfer of

energy to these. If enough energy is transferred, atoms are ionized generating the emission of secondary electrons (Secundary Electron (SE)) that are also important once they are emitted near of sample's surface, giving topological contrast information. Beyond SEs and BSEs, the interaction between the electron beam and the sample originates the emission of characteristic X-rays, auger electrons, cathodoluminescence photons, and some electrons can pierce the sample (transmitted electrons) [75][74], as it can be seen in fig. 3.5.

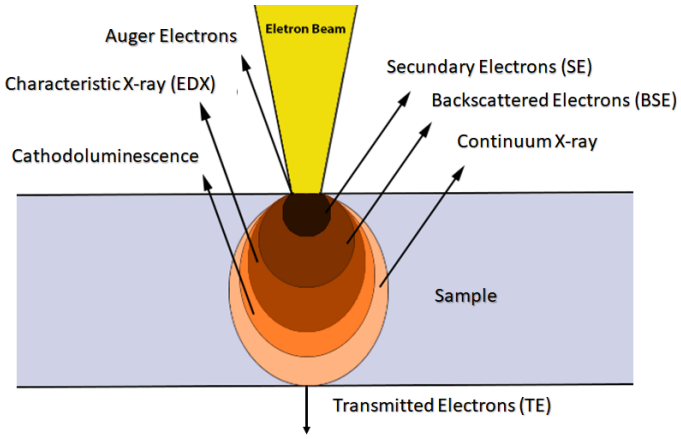

Figure 3.5: Schematic representation of interactions between beam electron and sample.

Due to the small spot from which SE emerges (close to the beam spot) and low energy, below 50eV, these electrons are easily attracted to the detector, usually an Everhart-Thornley detector, by applying a bias over the scintillator (+10 Kev) and over the Faraday cage (+200-300V). When electrons hit the scintillator, photons are generated that are photo multiplied and the output signal is proportional to the number of SE that emerge from the spot. Detectors of BSE like the Robinson detector are pretty similar to the Everhart Thornley SE detector but without a Faraday cage. Due to the fact that BSE can emerge far from the beam spot, the used scintillator has a hole that allows the beam to pass through and covers a large area. Typically BSE has enough energy to excite the scintillator without the need of applying a bias. This guarantees that SE isn't detected and the detector will not disturb the beam. The detector output is a signal proportional to the number of BSE that emerge from that spot [74].

Besides BSE and SE, X-rays are also emitted as a consequence of the interaction of the electron beam with the sample. This is the basis behind Energy Dispersive X-Ray spectroscopy and the reason why it is done in conjunction with SEM. When the electron beam hits the atoms, the electrons in the inner shell are ionized. Consequently, this empty hole left behind is filled by electrons from the outer layers with energy emission corresponding to the difference between the states involved in the transition. This energy is emitted in the form of a photon as is the case of the characteristic X-ray. As different atoms have different transition energies, the energy of characteristic X-rays can be associated with a specific atom. As the electron beam travels through the sample, these characteristic X-rays are detected and it is possible to identify the elements present. However, for elements with smaller atomic numbers, more energy is required to ionize them and so they are difficult to detect [76][77].

To analyze the sensors, the fibers were fixed to an aluminum holder using carbon tape and the SEM images were performed using the TESCAN Vega3 SB equipment at the Physics Department of the University of Aveiro, the SE were accelerated by a 15.0 kV bias. The detector used for EDS analysis was a Bruker Xflash 410 M Silicon Drift.

3.2.2 Raman Spectroscopy

Raman spectroscopy is a non-destructive technique that allows structural and chemical analysis of the phenomena of the interaction of light with matter. One of the major advantages is the ability to differentiate different atomic arrangements from the same atoms.

A simple model can be used to explain the phenomena used in Raman spectroscopy: analyzing a vibrating diatomic molecule that can be represented as two masses (atoms) bound by a weightless spring, is possible to define the vibrational frequency of the molecule as a function of the masses and the elastic constant. This oscillator model applied to quantum mechanics allows the determination of the well-defined vibrational energy states and an understanding of the molecular vibrations resulting from light interaction with matter. Due to this interaction, the sample's electrons are excited to unstable "virtual" energy states and quickly scattered to lower and more stable states, emitting a photon. If the initial and final states are the same, no energy is transferred to the sample and the emitted photon has the same wavelength as the incident one, through a process called Rayleigh scattering. If the initial and final states are different, some energy is transferred to the sample and the photon emitted has a different wavelength from the incident photon, in this case, the process is called Raman scattering. Inside Raman scattering, there are two different phenomena: when the final state is higher than the initial state is called Stokes Raman scattering; when the final state is lower than the initial state is called Anti-Stokes Raman scattering. These interactions are represented in the diagram of fig. 3.6. This energy transfer allows the molecule to experience different vibrational states, so Raman spectroscopy gives important information about these vibrations.

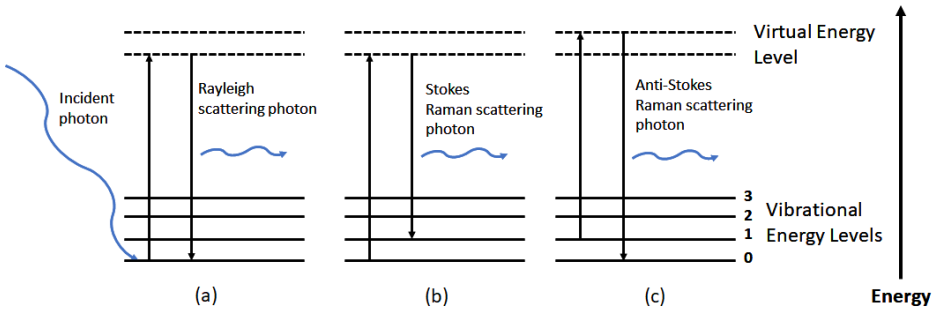

Figure 3.6: Diagram of (a) Rayleigh scattering, (b) Stokes Raman scattering, and (c) Anti-Stokes Raman Scattering.

Raman spectroscopy has proven to be a very versatile tool to analyze carbon allotropes, as it gathers information on the type of structure and, in the case of graphene and LIG, a semi-quantification of the number of layers and the presence of defects.

Graphene belongs to D_{6h} point group and in the center, Γ, of the Brillouin zone six normal modes occur: in-plane E_{1u} and E_{2g} (doubly degenerate); out-plane A_{2u} and B_{2g} (doubly degenerate) [78]. Graphene modes aren't ir-active once the two atoms per unit cell are equivalent and so the dipolar momentum is unchanged around the equilibrium position. However, E_{2g} mode is Raman active since the polarizability is altered. Although, multiple-layer graphene (MLG), like graphite, has four atoms per unit cell and in this case, non of the same plane two carbon are equivalent [78]. Now, the four modes become Davydov-doublets: E_{2g} create in-plane atomic displacement E_{1u} (ir-ative) and E_{2g} (raman ative) modes; B_{2g} creat out-plane atomic displacement A_{2u} (ir-ative) and B_{2g} (inative) modes; A_{2u} and E_{1u} creates rigid layer displacement B_{2g} (inative) and E_{2g} (raman ative) modes and two inative acoustic modes A_{2u} and E_{1u} [78]. As shown in fig. 3.7, the Raman spectrum of SLG and MLG are distinct due to the aforementioned Davydov-doublets enabling some to be Raman active. These characteristic peaks act as identifiers of graphene quality and are originated from the vibrations described above. The G peak (1580 cm^{-1}) is associated with sp^2 bonds stretching (E_{2g} mode). D peak (1350 cm^{-1} for 532 nm excitation) is related to the breathing modes of the aromatic rings and is forbidden by selection rules. However, these rules don't apply in graphene edges [79] and in the presence of defects [80]. Its overtone, 2D (2700 cm^{-1}), isn't forbidden once two phonons with symmetric momentum are part of the process complying with the selection rules [81]. These three peaks are the most intense ones but others can be seen on the Raman spectrum like D' (1580 cm^{-1}), also related to defects, and its overtone 2D' (4290 cm^{-1}). Two smaller peaks as a result of the mixing of the bands can also appear: D+D" (2450 cm^{-1}) and D+D' (2950 cm^{-1}) [81]. This zone from 1100 cm^{-1} to 3300 cm^{-1} is known as the "graphene fingerprint" due to the amount of information it provides but other bands beyond this region can be seen: 2D+G (4290 cm^{-1}) and C (30-50 cm^{-1}) [81].

The ratio between the intensity of the major bands can be also a useful tool to evaluate the defects and crystallinity and can give an estimate of the number of layers. The ratio I_D/I_G can provide an idea of the crystallinity, disorder, and defects, for high values the LIG presents many defects and low crystallinity [82][83]. On the other hand, the ratio I_{2D}/I_G gives information about the number of layers, as LIG have fewer layers for high values of I_{2D}/I_G [83]. However, it is also important to take into account the Full Width at Half Maximum (FWHM) since it can qualitatively complement the ratio analysis.

The Raman spectrums were acquired using a Raman 532 ER (Wasatch Photonics, USA) compact instrument, with a Cobolt 08-DPL (Hübner Group, Germany) 532 nm laser, from the Physics Department at the University of Aveiro. Acopolated to the system is an optical microscope (Olympus BH2-UMA) which was used in conjunction with a 100x lens with a NA of 0.8. The fibers were put into a holder and placed under the laser spot. Typically, the spectra were taken using 2 seconds integration with 10 accumulations using a laser output of 30 mW.

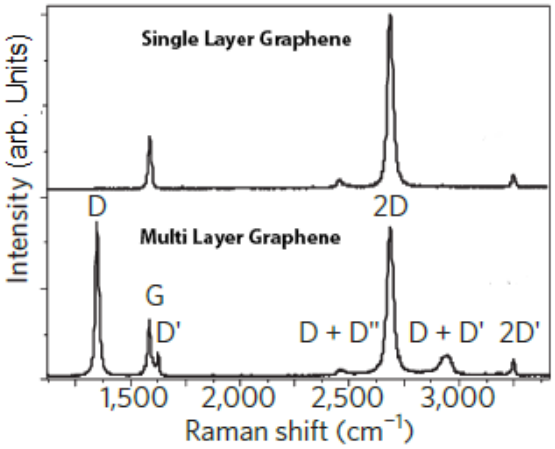

Figure 3.7: Raman spectrum of single layer graphene (SLG) (top) and defected multiple-layer graphene (MLG), adapted [81].

3.2.3 Attenuated Total Reflectance Fourier-Transform Infrared Spectroscopy (ATR-FTIR)

Raman and FTIR are complementary techniques used to characterize molecular composition and structure. In FTIR, the interaction between Infra-Red (IR) light and the sample originates the absorption or transmission of some frequencies that are recorded in an IR spectrum. This spectrum shows the absorption bands of the sample relative to the functional groups and structure. Furthermore, the peak's intensity is proportional to the quantity of these functional groups giving qualitative information about the sample's composition. This technique is versatile as it can be used to analyze gases, solids, and liquids [84].

IR radiation isn't energetic enough to produce electronic transitions. However, molecules can absorb some of this energy in the form of changes in dipolar momentum related to vibration or rotations. A molecule's potential to change its position is defined by its degrees of freedom. Considering a molecule with N atoms, it has 3N total freedom degrees of which 3 describe translations and another 3 describe rotations (2 in the case of a linear molecule). Thus the remaining 3N-6 (3N-5) describe vibrations [85]. Among the most common types of vibration are: symmetric and asymmetric stretching related to the changes in inter-atomic bonding distance; changes in the angle between bonds like in-plane rocking and scissoring, and out-plane wagging and twisting.

In fig. 3.8 a schematic representation of an FTIR spectrometer is shown. The light that is emitted from the light source is divided into two equal beams by a beam splitter. One of the beams travels to a fixed mirror while the other travels to a moving one. After being reflected they recombine in the beam splitter. This Mach Zehnder configuration allows, depending on the position of the moving mirror, different frequencies to constructively interfere generating an interferogram. The light then travels through the sample, where the frequencies relating to the vibrations are absorbed and the rest is transmitted and recorded by the detector in the form of the interferogram. A computer applies the FT method to convert the interferogram into an IR spectrum to acquire the intensity of individual frequencies.

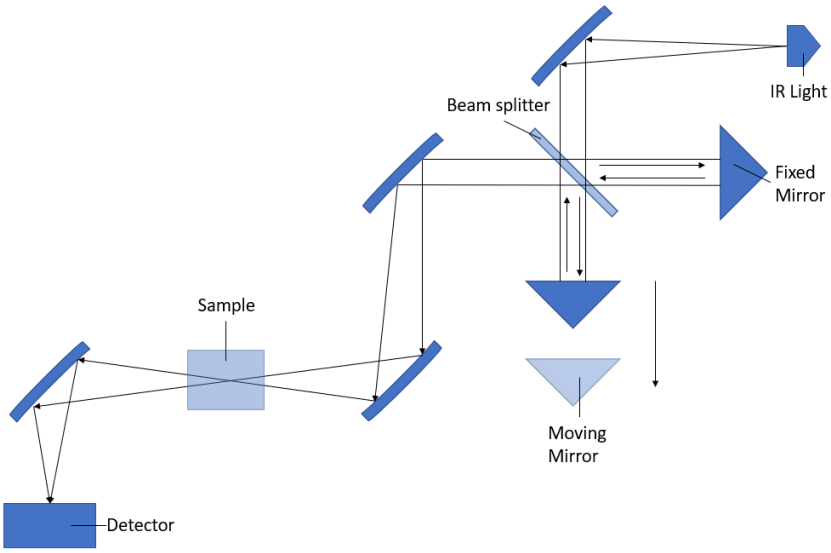

Figure 3.8: Schematic representation of an FTIR device.

In some cases, the preparation of samples and spectrum acquisition can be challenging to perform under a conventional FTIR spectrometer. Due to that, a more versatile sample-managing technique was developed. The ATR-FTIR method uses the TIR phenomenon to generate an evanescent wave that interacts with the sample. The IR radiation travels across an ATR-FTIR crystal (diamond, ZnSe or Ge [86] [87] [88]) that is in contact with the sample. The incidence angle needs to be greater than the critical angle to fulfill TIR conditions. The evanescent wave created will be altered or attenuated in regions of the IR spectrum where the sample absorbs energy. These changes are measured and displayed as a spectrum.

The fibers were placed in the ATR-FTIR holder and compressed with the crystal to achieve the TIR. The equipment used was a IR spectrometer (Brunker Alpha Platinum, Germany with a crystal of diamond), with a 4 cm^{-1} resolution and 32 scan sweep from the chemistry Department at the University of Aveiro. During the analysis, the room temperature was 23° and 35% of humidity.

3.2.4 Optical measurements

The FPI sensors described in section 3.1.1 were submitted to strain, temperature, and RI tests. For the strain tests, the fibers were glued into two supports (the glue points were separated by 50 mm), one of which was a linear positioner that allowed the fiber to be stretched at 2 μm steps, from 0 to 8 μm, and, back. The reflection spectrums were collected using the interrogator and the data were analyzed on Origin. For the temperature tests, the fibers were placed inside a thermal chamber and the temperature was increased in 5°C steps from 25°C to 45°C and the reflection spectrum was acquired using the interrogator. For RI analysis, firstly, eighth glucose concentrations were prepared using D-(+)-glucose ($\geq$ 99.5) from Sigma-Aldrich, and their RI were determined using a refractometer (Abbemat 200, Anton Paar), obtaining 1.333, 1.334, 1.339, 1.346, 1.359, 1.368, 1.378, 1.387 RIU for 0, 1, 5, 10, 20, 30, 40 and 50 % (w/v) glucose solutions, respectively. After that, the fibers were

cleaned with DI water (Milli-Q water purification system) and immersed in each solution for three minutes, acquiring the reflection spectrum at the end.

For cortisol detection, 0, 0.01, 0.1, 0.5, 1, 2, and 3 ng/mL solution of cortisol (Sigma-Merck) were prepared. A stock solution was made using 1 mg of cortisol dissolved in 100 μL of ethanol and in 10 mL of PBS (pH=7.4, 10 mM, Fisher Bioreagent). This 0.099 mg/mL solution was diluted into the concentration described above. All the fibers were initially cleaned with PBS and then immersed in each solution for 5 minutes, taking the reflection spectrum at the end. Also, the selectivity for cortisol was tested, for this propose four solutions with 3 ng/mL of glucose, fructose (Himedia, 99-102%), sucrose (JMGS, LDA, 1 kilo), and, ascorbic acid (L-Ascorbic Acid from Fisher Chemical, $\geq$ 99%) were prepared using the same process described above. In the end, the FPI response was tested to pH using a solution of acetic acid (pH3, Fisher Chemical, $\geq$99.7%), ethanol (pH6), and, potassium hydroxide (pH10 and pH14, Fisher Chemical, $\geq$85.0%), for this one, two different concentrations were prepared. For all the solutions, the pH was measured with a strip of litmus paper.

Finally, ammonia (LabKem, 0.9Kg/L) solutions of 0, 100, 200, 300, 400, 500, 600, and, 700 ppb were prepared for the detection. Firstly, an ammonia stock solution of 7000 μg/L or 7000 ppb was prepared by diluting 78 μL of ammonia in 9.922 mL of DI water. This solution was later diluted in DI water to make all of the intended solutions. The fibers were initially cleaned with DI water and then immersed in each solution for 5 minutes, recording the reflection spectrum at the end. The experimental setup for testing the FPI is represented in fig. 3.9.

All experiments were carried out at a temperature of approximately 21°C.

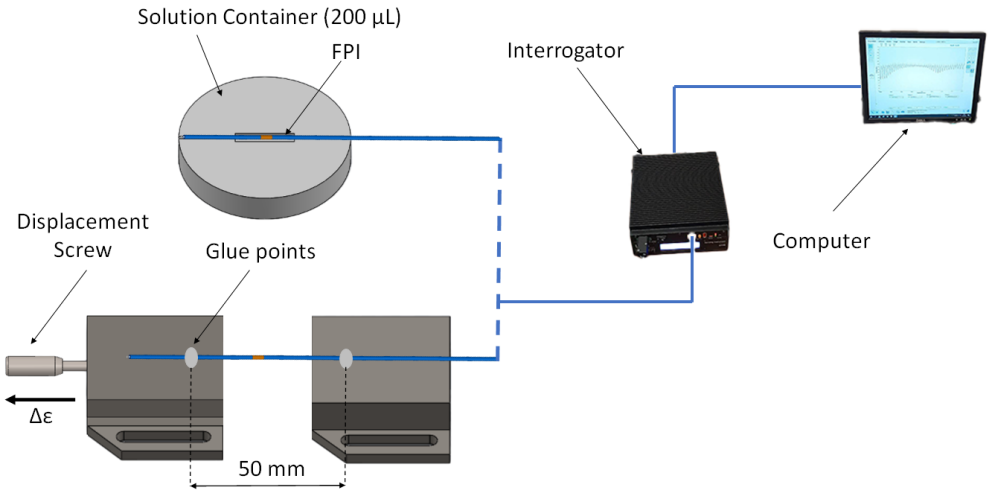

Figure 3.9: Schematic representation of the experimental setup used for testing the FPI.

— 4 —

Results and Discussion

4.1 Optical Analysis

The FPI fabricated by the process described in section 3.1.1 were submitted to strain, temperature, and, RI tests to evaluate their response to external stimuli.

4.1.1 FPI Analysis Before LIG Inscription

Firstly, FP1, FP2, FP3, FP4, FP5, and, FP6 were submitted to stretching tests and the results are presented in fig. 4.1.

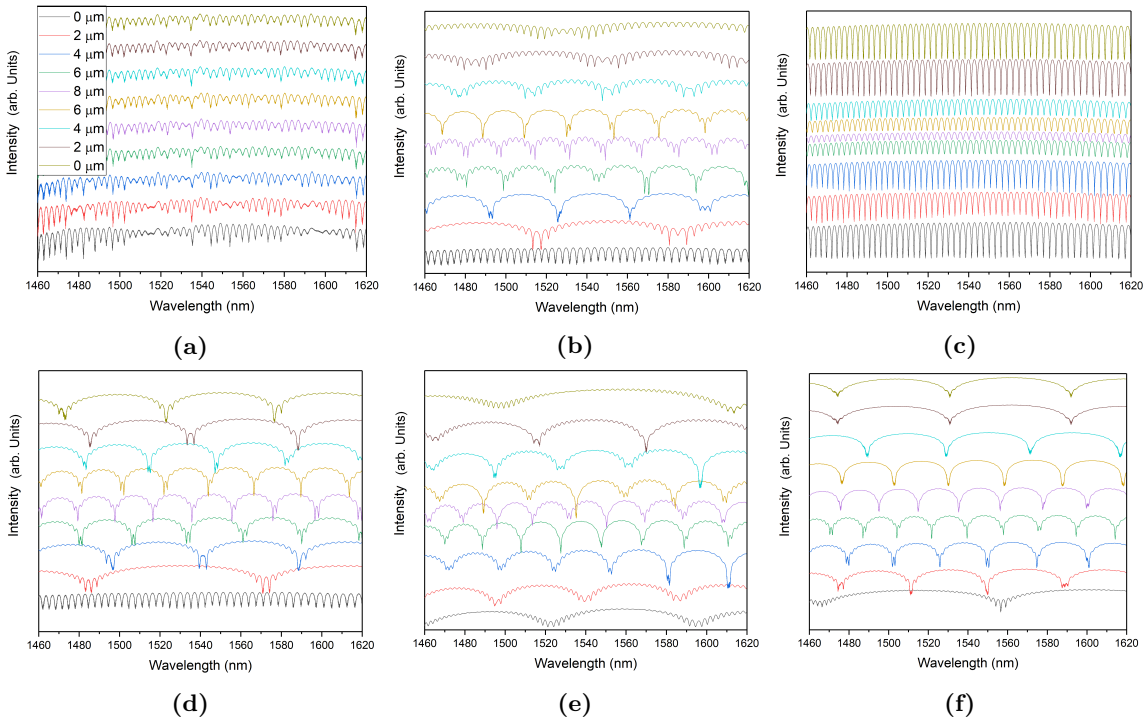

Figure 4.1: Strain reflection spectrum of (a) FP1, (b) FP2, (c) FP3, (d) FP4, (e) FP5 and (f) FP6.

As is possible to observe, two different phenomenons occur: while the reflection spectrum of FP1 and FP3 just shifts, the spectrum of FP2, FP4, FP5, and FP6 changes considerably,

occurring a kind of coupling between two signals. Due to the distensive forces applied, a second cavity could appear between SMF and PI and justify this phenomenon, as shown in fig. 4.2a. In this case, a void cavity and the polyimide cavity would make up the interferometer, achieving a Vernier effect, as discussed above in section 2.1.3. However, the two cavities produce signals with different FSR, since both the RI and the length of the cavities are quite different. This implied that the modulation obtained is different from the beat-like signal, fig. 2.6, that normally occur with Vernier effect. To prove this hypothesis, the Vernier effect was simulated in the case where the FSR of the signals are 25 times different. As can be seen in fig. 4.2b, for signals with a huge period difference, the effect obtained is similar to the one identified in the FP2, FP4, FP5, and FP6 spectra, proving the suggested hypothesis. Although this phenomenon has amplified the sensitivity, the used equipment does not cover a sufficient wavelength range to follow the variation. Nevertheless, the analysis of the signals is quite complex because the constant stretching caused by the strain tests makes the size of the cavity vary during the whole test, altering consequently the FSR of the Vernier envelope. It was concluded that when this phenomenon happens it is not possible to analyze the strain sensitivity of the sensor.

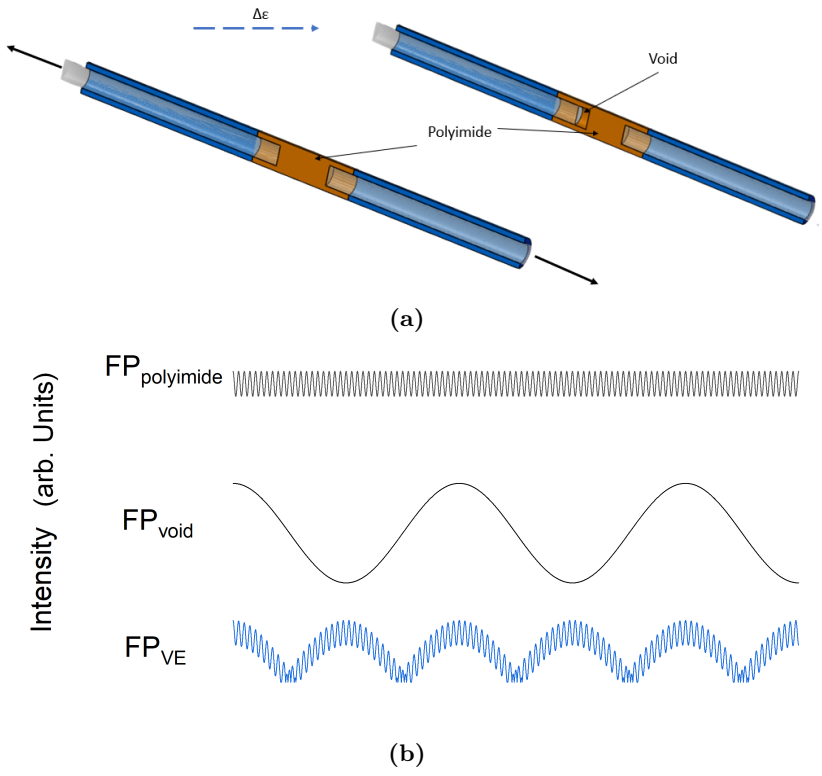

Figure 4.2: (a) Schematic representation of the void creation during the strain tests; (b) Simulation of the Vernier effect applied to the FP_{void} and $FP_{polyimide}$ case.

Only in the FP1 and FP3 interferometers did not occur the void phenomenon, and for these FPI, a peak was then monitored during the tests. A redshift was observed with the applied strain and a blueshift when the strain was relieved. The experimental points obtained

are represented in the graphs of fig. 4.3. The FP3 sensibility was higher when compared with FP1, with 4.5 pm/$\mu\varepsilon$ and 1.9 pm/$\mu\varepsilon$ during the increase of strain, respectively, and with 6.0 pm/$\mu\varepsilon$ and 2.3 pm/$\mu\varepsilon$ during the decrease of strain, respectively. These results are of the same order of magnitude as those discussed in section 2.1.2.

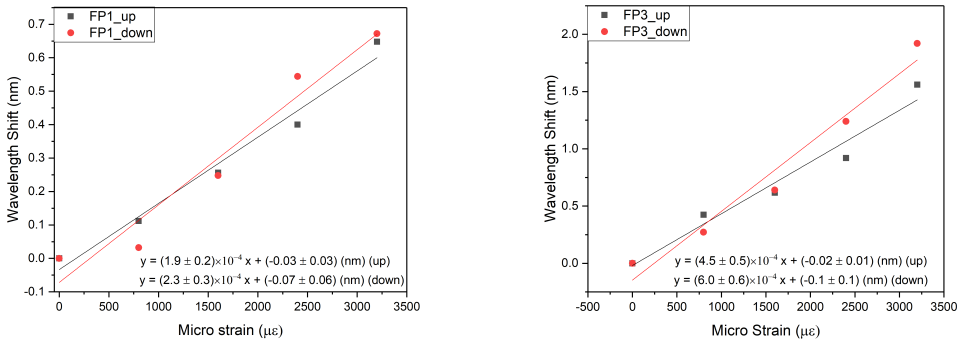

(a) **(b)**

Figure 4.3: Strain test for (a) FP1 and (b) FP3 interferometers.

As mentioned, the FPI were also subjected to temperature and refractive index tests. The graphs in fig. 4.4a and fig. 4.4b represent the wavelength shift of a given peak when submitted to a temperature and refractive index variation, respectively. The behavior of the interferometers for temperature was identical, observing a blueshift with increasing temperature. This effect can be explained by the increase of the cavity length due to the thermal expansion induced in the PI during the test. When it comes to the RI test, a redshift is observed with increasing refractive index.

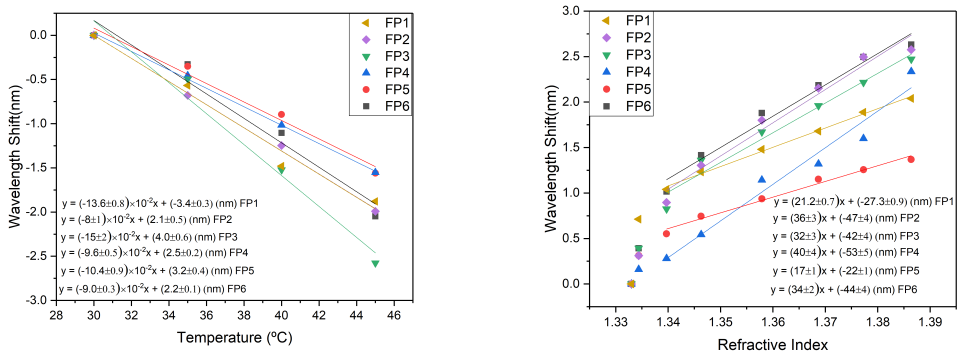

(a) **(b)**

Figure 4.4: (a) Temperature and (b) RI sensibilities of FP1, FP2, FP3, FP4, FP5, and, FP6 interferometers.

All sensitivities are summarised in table 4.1 and the interferometers were sorted by cavity length to associate them with the experimental results. Apart from FP1 and FP5, it is possible to observe a slight trend where the temperature sensitivity is proportional to the length of the cavity. On the other hand, the presence of AuNPs in the cavity seems to increase the sensitivity to the refractive index. This result deserves further investigation in order to confirm this trend and to understand what mechanisms are behind this improvement. It

should be noted that the manufacturing process can change the interferometer characteristics, once the thickness of the PI layer that surrounds the FPIs is difficult to control using the current processes and can influence the results.

Table 4.1: Strain, temperature and RI sensibilities for each FPI ordered by cavity length.

	Gap (μm)	**Gap Material**	**Strain (pm/$\mu\varepsilon$)**		**Temperature (pm/°C)**	**RI (nm/RIU)**
			Up	**Down**		
FP1	105	PI	0.19	0.23	-136	21.2
FP2	125	PI AuNPs	-	-	-80	36
FP6	172	PI	-	-	-90	34
FP4	175	PI AuNPs	-	-	-96	40
FP3	182	PI AuNPs	0.45	0.6	-150	32
FP5	218	PI	-	-	-104	17

The sensitivities obtained for the interferometers vary from -136 to -80 pm/°C and from 17 nm/RIU to 40 nm/RIU to temperature and RI response. These results are not very interesting when compared with those reported in [37][38][39][28], however, one of the objectives of this work is to observe and study the transformation of the polyimide in LIG and the influence this process has on interferometers and their sensitivities.

4.1.2 LIG Inscription

To find the laser parameters that result in better LIG quality, some fibers coated with polyimide (SM1250(10.4/125)P) were used to do the tests. The parameters evaluated were the power (%) (note that in fig. 3.2b is presented the calibration curve of the laser used) and the scribing velocity (mm/s) maintaining the pulse frequency at 20 kHz, the samples were named as "power_velocity" for further analysis. In fig. 4.5a is presented the Ramam spectrum of each sample. As it is shown, the D (1345 cm^{-1}), G (1584 cm^{-1}), and 2D (2690 cm^{-1}) bands are well defined for every fiber, and, also in some cases is possible to notice the D' (1613 cm^{-1}) and D + D' (2934 cm^{-1}) bands. This allows already to realize that the LIG formed is of good quality.

Furthermore, as it was said above in section 3.2.2, the ratios I_D/I_G and I_{2D}/I_G give information about the LIG crystallinity, the presence of defects and the number of layers. The ratios presented at table 4.2 show values between 1.142 and 0.922 (A.U.) of the I_D/I_G ratio, which possibly means that the LIG produced has a high density of edges. This can occur due to the high laser fluence, as the powers used in this experiment vary from 10 to 20 W, approximately. This implies that the gas released from the photothermal process occurs rapidly, making the LIG very porous with many graphene edges. For the I_{2D}/I_G ratio, were obtained high values as well, from 0.804 to 0.966 (A.U.), this means that the LIG produced has a low number of graphene layers. In [89], where the I_D/I_G ratio was about 0.95 (A.U.) similar to the results of this work, the LIG exhibit a porous morphology. Furthermore, the I_{2D}/I_G ratio was as lower as 0.62 (A.U.) which means that the LIG synthesized in this work have

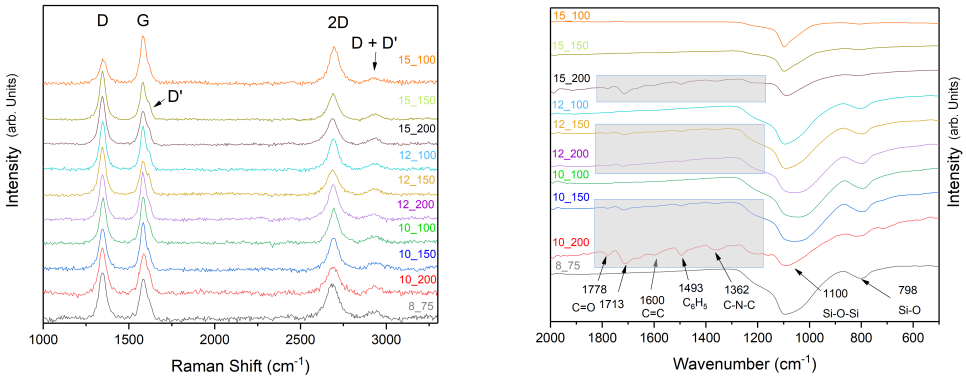

(a) **(b)**

Figure 4.5: (a) Ramam and (b) FTIR spectra of fibers that have undergone different laser output powers and different scribing velocities (The blue zone correspond to the vibration band related to PI).

few graphene layers (for values between 0.8 and 1.8 the LIG contains 10 or fewer graphene layers [90]). The ratios, however, obtained for each combination of parameters don't show a tendency related to the variation of the power or the variation of the velocity. Furthermore, is perceptible that the decreasing velocity reduces the D and 2D bands FWHM, which means that LIG presents a more ordered and crystalline structure. Also, fibers irradiated with 8 and 15 % of power show higher FWHM values, having a less ordered structure.

Table 4.2: I_D/I_G, I_{2D}/I_G ratios, FWHM of D and 2D bands for the different scribing speed and power combinations.

I_D/I_G		Power (%)				I_D/I_G		Power (%)			
		8	**10**	**12**	**15**			**8**	**10**	**12**	**15**
Velocity (mm/s)	**75**	1.142	-	-	-	**Velocity (mm/s)**	**75**	0.960	-	-	-
	100	-	0.997	1.023	0.922		**100**	-	0.915	0.937	0.964
	150	-	0.936	1.088	1.047		**150**	-	0.839	0.946	0.955
	200	-	1.089	0.986	1.071		**200**	-	0.804	0.916	0.966
D Band (FWHM) (cm^{-1})		Power (%)				**2D Band (FWHM) (cm^{-1})**		Power (%)			
		8	**10**	**12**	**15**			**8**	**10**	**12**	**15**
Velocity (mm/s)	**75**	56.1	-	-	-	**Velocity (mm/s)**	**75**	100.1	-	-	-
	100	**-**	48.6	47.4	55.6		**100**	**-**	74.8	71.4	77.6
	150	**-**	54.4	50.0	47.5		**150**	**-**	117.9	84.4	74.2
	200	**-**	56.6	49.0	49.2		**200**	**-**	97.1	82.4	84.9

Another important parameter that needs to be taken into account is the thickness of the LIG layer. For that purpose, a FTIR analysis was performed and the results for each fiber are presented in fig. 4.5b. As the fiber is compressed until it breaks, the entire fiber content is analyzed, and is possible to conclude if all the PI was or was not transformed into LIG. As is shown, all the fibers present a wide band at 1100 cm^{-1} and another one at 798 cm^{-1} associated with Si-O-Si asymmetric stretching and Si-O stretching vibration, respectively [91], related with the presence of silica from the core's fiber. For some fibers is also visible other vibration bands, in this case, due to the presence of polyimide. The bands at 1778 cm^{-1} and 1713 cm^{-1} are the symmetric and asymmetric C=O vibration, respectively [92][56]. The band at 1600

cm^{-1} is related to benzene ring C=C stretching [92], 1493 cm^{-1} is associated with the stretch of the phenyl groups (C_6H_5) [56], and the 1362 cm^{-1} band is the imide ring C–N–C stretching [56][92]. The presence of these bands indicates that not all the polyimide was transformed into LIG, this happened with all the fibers that were inscribed with speeds of 150 and 200 mm/s. On the other hand, the fibers inscribed with 100 mm/s do not present any bands related to PI.

Taking into account the Ramam and FTIR analysis was concluded that the best parameters to use on LIG inscription were velocities under 100 mm/s for any power output. However, the laser power can be a little unstable for values under 10% and can also damage the fiber when the power used is 15%, as it was possible to observe during the tests. For this reason, 10% and 12% power outputs for 100 mm/s scribing velocity were the chosen parameters.

The selected fibers were also submitted to SEM in order to examine the fiber's cross-section and surface. In fig. 4.6a and fig. 4.6b can be observed that the cross-section of both fibers has two distinct structures: a circular one that corresponds to the fiber's cladding and another that surrounds it that corresponds to the LIG layer. Note that the cross-section cut left marks on the fiber. The EDS map of these images is present in fig. 4.6c and fig. 4.6d which shows that the circular structure is composed of silicon atoms, corresponding to the cladding, and the structure surrounding it is composed of carbon atoms, corresponding to LIG layer. From these images no layer is identified around the cladding that could be associated with the PI not transformed into LIG, suggesting that the entire PI coating has been transformed into LIG. Note that the presence of carbon on the cladding surface is due to the imperfection of the cut.

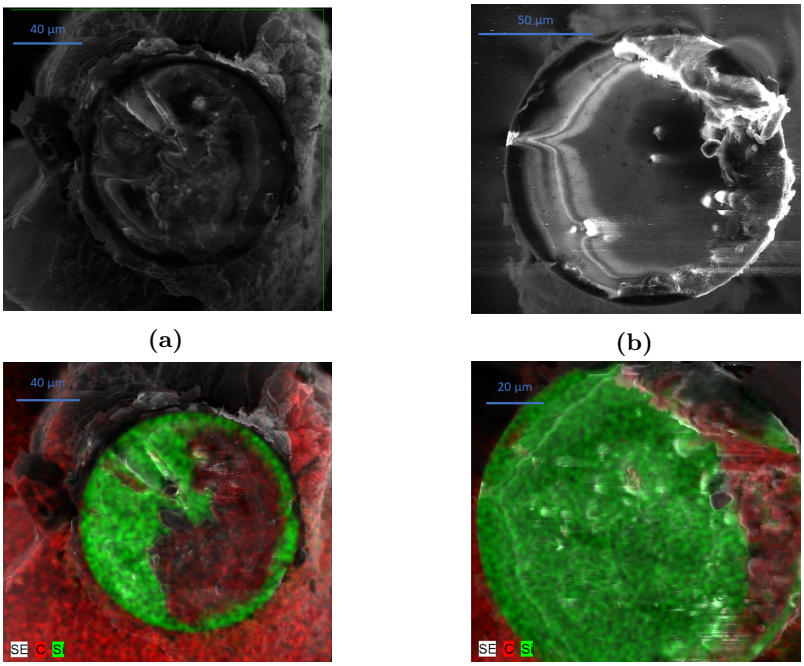

(a) **(b)** **(c)** **(d)**

Figure 4.6: (a) SEM image of the cross-section of the fiber 10_100; (b) SEM image of the cross-section of the fiber 12_100; (C) EDS map of the cross-section of a fiber 10_100; (d) EDS map of the cross-section of a fiber 12_100.

Concerning the surface of the fibers, it is possible to observe from the images of the fig. 4.7 that the LIG formed is quite porous as expected, has a leafy texture and is quite homogeneous along the length of the fiber. Compared to the results presented in [56] and [18], the formed LIG presents a greater homogeneity, besides not presenting the substructures found in those works. The pulsed laser used in this work has a great influence in obtaining these characteristics.

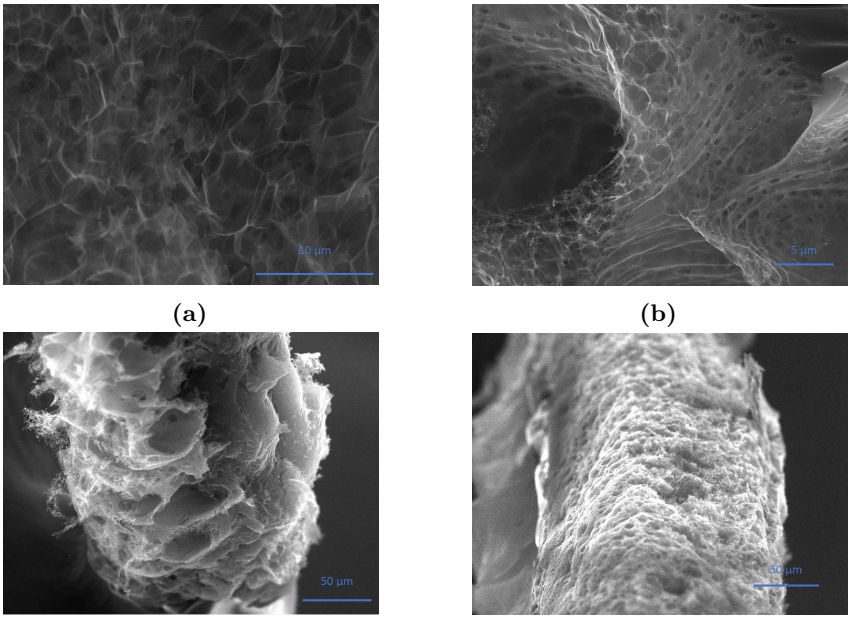

(a) **(b)**

(c) **(d)**

Figure 4.7: (a) SEM images from the 10_100 fiber surface; (b) SEM images from the 12_100 fiber surface; (c) and (d) less applied SEM images of the 10_100 fiber surface from different sides.

Although the results presented by the 10_100 and 12_100 fibers are identical, the fibers inscribed at 10% power seem to have a greater homogeneity. For that reason, the parameters chosen were 10% power and 100 mm/s of scribing velocity for the inscription of LIG in the interferometers.

Using these parameters for the inscription of LIG, the interferometers were then subjected to the laser. Spectra were taken before and after each inscription, in which the cavity is rotated 90° between each inscription, and can be seen in the graphs in fig. 4.8. Unfortunately, interferometers FP3, FP4, and FP6 were destroyed in this process. After the first scribing, all FPI's reflection spectra lose some intensity. This is possibly due to the penetration of the laser into the Fabry-Perrot cavity, transforming part of the polyimide that composed it into LIG and preventing a fraction of the light that previously propagated through the cavity from now being propagated. After each scribing, the spectra change dramatically, but at the end of the inscription process all spectra show some similarities. As it is possible to observe, a similar phenomenon to the one described for the strain tests occurs. A second cavity is created due to the formation of LIG inside the polyimide cavity leading to the Vernier effect. Also, in this case, the difference between the FSR of the two cavities is too different to observe a beat-like

signal. Fig. 4.9 presents a schematic representation of the FPI longitudinal cross-section after LIG inscription, a second cavity is created around the polyimide, this configuration can be seen as two FPI in series. It is also important to mention that the penetration of the LIG layer in the polyimide cavity is greatly influenced by the thickness of the interferometer, as already discussed, the current manufacturing process of FPI does not allow uniformity of its thickness. This is why the intensity of the fringes has decreased and the intensity of the Vernier envelope has increased more for some interferometers than others. There is no uniformity in the thickness of the cavities, so the intensities differ.

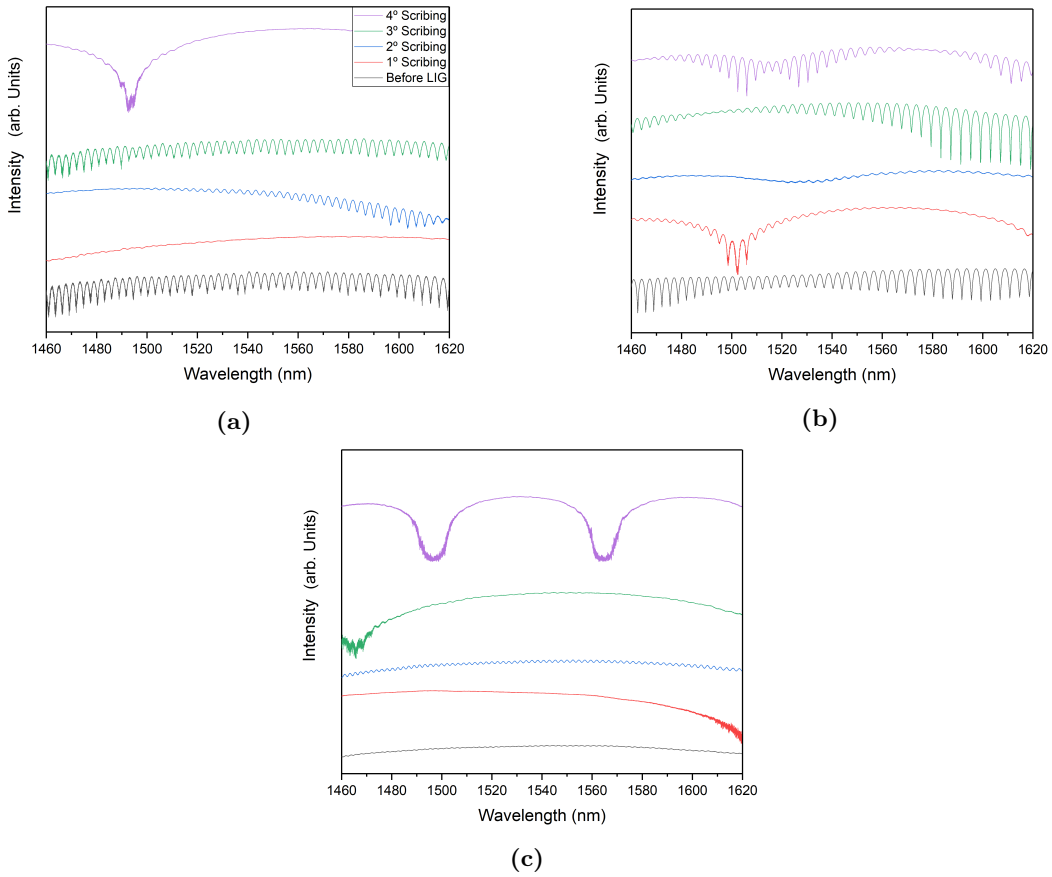

Figure 4.8: Reflection spectrum before and after each scribing of (a) FP1, (b) FP2, and, (c) FP5.

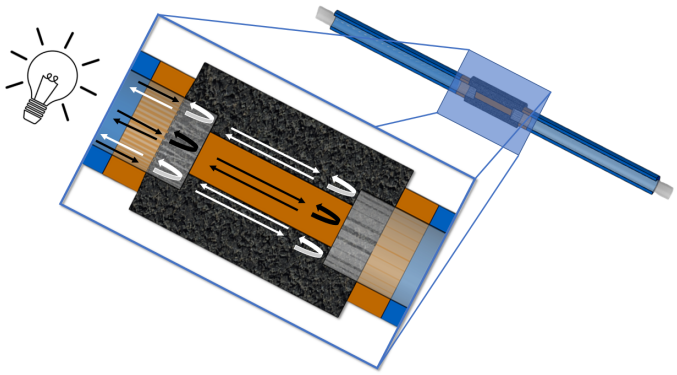

Figure 4.9: Schematic representation of the longitudinal cross-section of the interferometer after LIG inscription (white arrows - light related with the interaction with LIG; black arrows - light related with the interaction with PI).

4.1.3 FPI Analysis After LIG Inscription

After LIG inscription, the FPI were submitted to RI tests again and the results are shown in fig. 4.10. A blueshift is observed with increasing refractive index, this effect is similar to the enhanced Vernier effect identified in fig. 2.7c, where the Vernier envelope moves in the opposite direction to the original interferometer. Note that with the immersion of the interferometer, the solution is diffused into the pores of the LIG layer changing the RI of the cavity. As can be seen in fig. 4.11, the FPI sensitivities show values ranging between 180 and 2600 nm/RIU much higher than those recorded before the formation of LIG. In fact, the magnification values record in table 4.3 vary between -8.5 and -153 (A.U.). It is also possible to see that the sensitivity is higher as the size of the gap increases. These results show that the interferometers are quite sensitive to the variation of the RI, which can be used as a mechanism to detect analytes. As was presented in the section 2.3.1, the RI changes at the metallic surface are used as a detection mechanism. The same principle can be used for this FPIs to possibly detect cortisol and ammonia.

Table 4.3: RI sensibilities before and after LIG inscription and correspondent M factor.

	Gap (μm)	**Gap Material**	**RI Sensibility (nm/RIU)**		**M Factor (A.U.)**
			Before LIG	**After LIG**	
FP1	105	PI	21.2	-180	-8.5
FP2	125	PI AuNPs	36	-450	-12.5
FP5	218	PI	17	-2600	-153

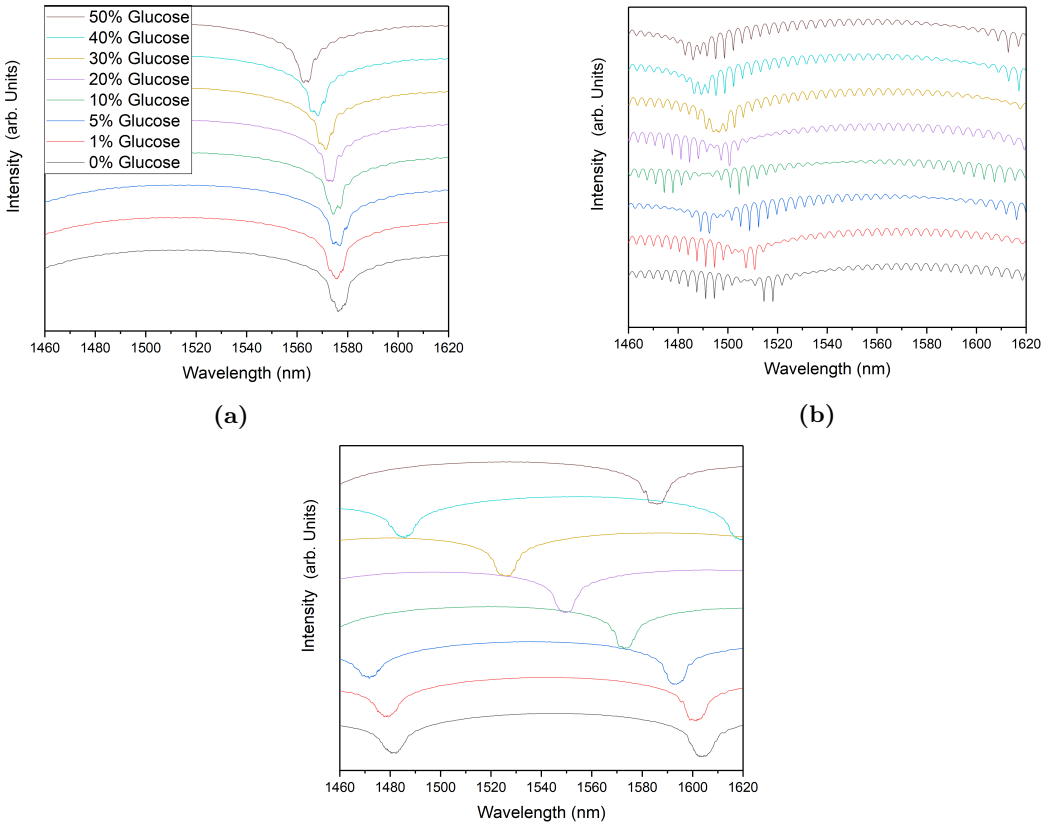

Figure 4.10: RI test after LIG inscription for (a) FP1, (b) FP2, and, (c) FP5 interferometers.

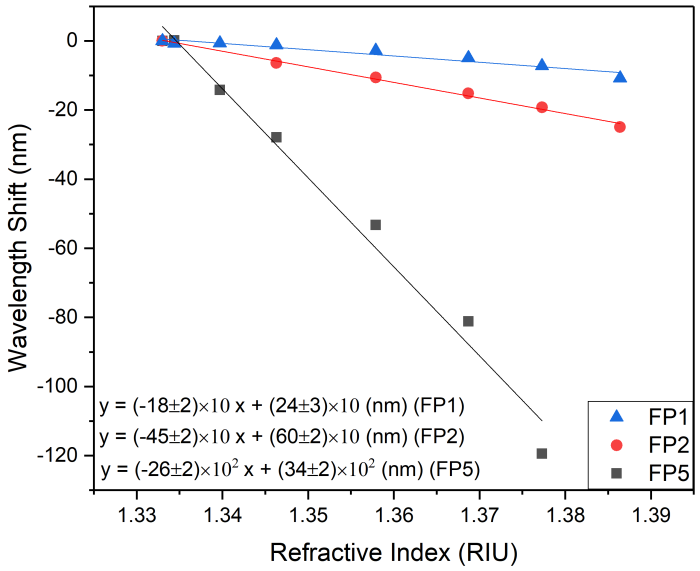

Figure 4.11: RI sensibility after LIG inscription for FP5, FP6, and, FP9 interferometers.

4.2 Potential Applications for Aquaculture Water Monitoring

After realizing that interferometers are very sensitive to refractive index variations, it was decided to functionalize the LIG layer to give it affinity for cortisol.

4.2.1 Cortisol Functionalization and Detection

The functionalization was performed on interferometers FP1 and FP2 following the process described in section 3.1.4 while interferometer FP5 and FP9 (FPI without LIG inscription) were used as a control. After each step, the reflection spectrum was recorded, as is possible to see in the graphs of fig. 4.12. At first, the Vernier envelope is blue-shifted by the application of MPTMS, then redshifted when the interferometer is immersed in solutions of AuNPs and MUA, and blueshifted again by the EDC/NHS and antibody steps. The drastic change in the spectra is seen as a good indication regarding the immobilization of the cortisol antibody.

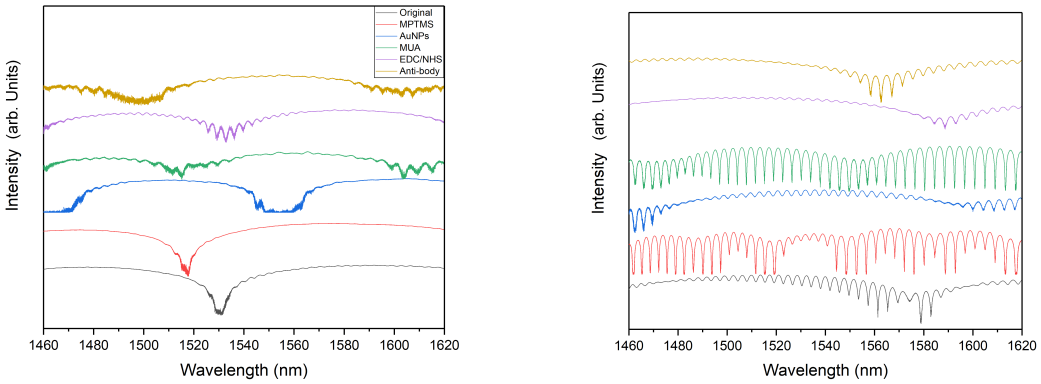

Figure 4.12: Reflection spectra of (a) FP1 and (b) FP2 before and after each functionalization step.

To prove that the functionalization of cortisol was successful, PI coated fiber, functionalized PI coated fiber, LIG coated fiber, and functionalized LIG coated fiber were submitted to FTIR and the results are presented at fig. 4.13. The PI coated fiber (black line) just presents bands associated with the bonds between the atoms that compose polyimide as discussed above. In comparison, the functionalized PI coated fiber (red line) presents the same bands but with slightly more intensity. Furthermore, vibration bands at 1640 and 840 cm^{-1} appear, the first one was associated with the amide bonds present at AuNPs surface after the functionalization [93][94], and the last was also associated with the AuNPs presence [95]. At low wavenumbers, appear at 635 and 600 cm^{-1} two bands that can be related to the presence of proteins [96][97], as the antibody is composed of proteins, it is possible to associate these bands with the immobilization of the antibody on the fiber surface. These results show that the functionalization process occurs successfully. For the fibers coated with LIG, the same conclusions can be taken. The functionalized LIG coated fiber (green line) shows bands associated with C=O, C=C, and C-H that fiber solely coated with LIG (blue line) does not present. Also, shifts at 1707 and 798 cm^{-1} can be related to the functionalization process. In both PI and LIG coated fibers the cortisol antibody was immobilized with success, helping to corroborate the results.

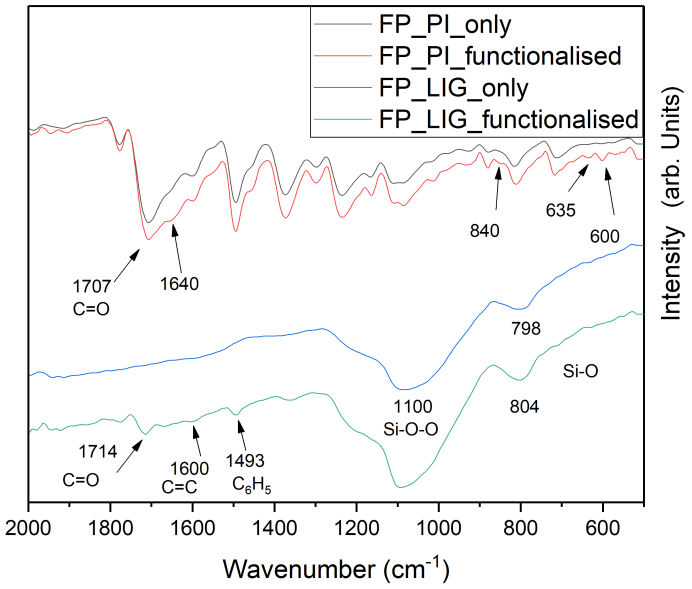

Figure 4.13: FTIR spectrum of PI coated fiber, functionalised PI coated fiber, LIG coated fiber and functionalised LIG coated fiber (from top to bottom).

The graphs presented in fig. 4.14 shows the cortisol tests, is possible to notice a redshift with the increase of cortisol concentrations. As hypothesized, the chemical reactions between the antibody and the cortisol altered the refractive index of the cavity and as a consequence, the spectra underwent a shift.

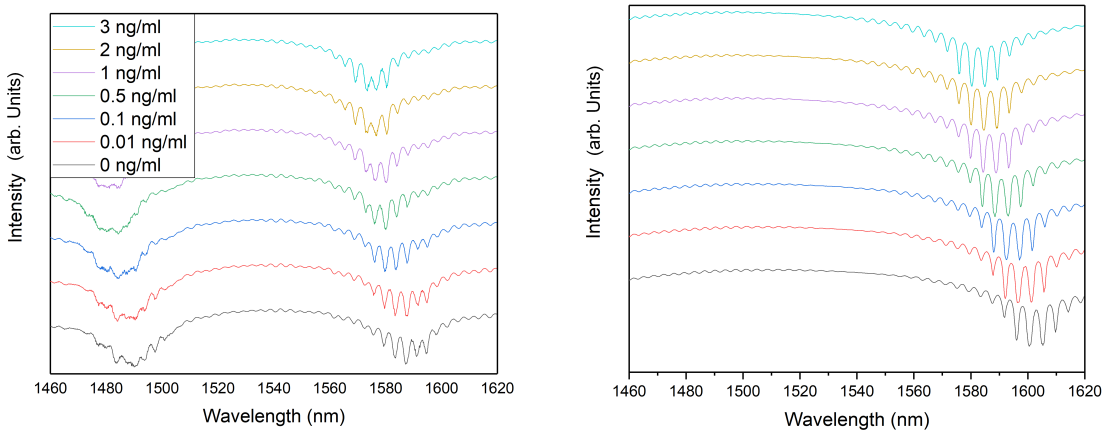

Figure 4.14: Cortisol tests of (a) FP1 and (b) FP2 interferometers.

Also, the interferometers FP5 and FP9 were tested and the results of the sensor's sensibilities are shown in the graph of fig. 4.15 and are sumarized in table 4.4. Regarding FP9 no significant deviation in the spectra was observed as expected with a sensibility of 0.029±0.007 nm/log(ng/mL), however, in the case of a non-functionalized LIG coated interferometer, FP5, a sensibility of -2.4±0.6 nm/log(ng/mL) was recorded but without much linearity (R^2=0.8), this response to cortisol may be related to the high sensitivity of this interferometer to RI.

Nevertheless, it is smaller than the sensibilities recorded for the functionalized interferometers. In this case, sensibilities of -4.1±0.2 nm/log(ng/mL) and -34±5 nm/log(ng/mL) were achieved for FP1 and FP2, respectively. There seems to be an increased sensitivity due to the presence of AuNPs in the FP2 cavity. One possible explanation is that because of this presence, there will be more AuNPs available to be functionalized, and then cortisol sensitivity will be improved. However, further studies should be developed to understand the influence of AuNPs on these results. FP2 was also submitted to a second test showing a sensitivity of -5.9±0.6 nm/log(ng/mL) denoting a decrease in sensitivity as a consequence of the decrease in the number of unbound antibodies available. The results obtained show an increase of up to 50 times in sensitivity when compared with other cortisol sensors [62]. The enhanced sensitivity recorded for interferometers FP1 and FP2 compared to FP5 and FP9 shows that the functionalization process and has a strong influence on the results.

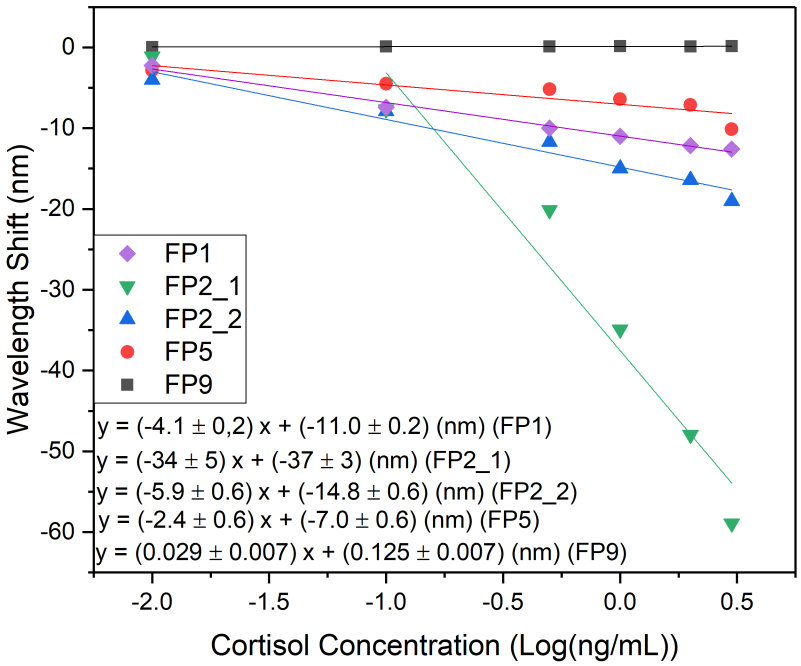

Figure 4.15: Cortisol test for FP1, FP2, FP5, and, FP9 interferometers.

Table 4.4: FP1, FP2, FP5, and FP9 gap, gap material, last procedure, and sensibilities for cortisol.

	Gap (μm)	**Gap Material**	**Last Procedure**	**Cortisol Sensibility (Log(ng/mL))**
FP1	105	PI	Functionalization	-4.1
FP2	125	PI AuNPs	Functionalization	-34
FP5	218	PI	LIG inscribing	-2.4
FP9	157	PI	PI Filling	0.029

The FP2 interferometer was also tested for selectivity since in a real environment, i.e. aquaculture water, there are other compounds that may interfere with cortisol detection, so

was tested the sensor's behavior to glucose, sucrose, fructose, and ascorbic acid presence, the results are shown in fig. 4.16a. The sensor proved to be immune to other substances and the observed deviations are essentially due to the change of refractive index of the medium with the dissolution of the interferents. For this same reason, the sensor proved to be very sensitive to pH changes, as possible to observe in fig. 4.16b, since the solutions have different refractive indices.

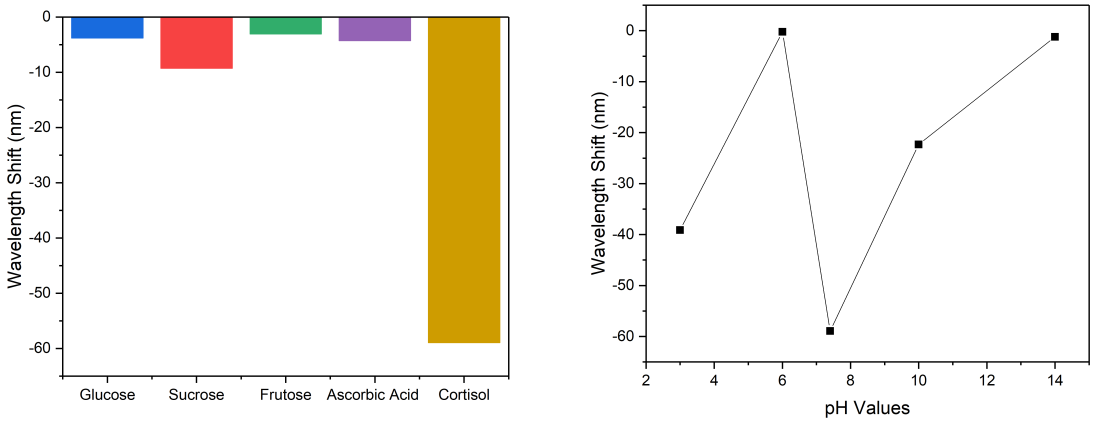

Figure 4.16: (a) Selectivity and (b) pH tests for FP2 interferometer.

4.2.2 Ammonia Detection

FP8 interferometer before and after LIG inscription and FP10 were used for ammonia detection. As described in section 3.1.5 this interferometer had oxazine 170 perchlorate mixed with its polyimide. The results in fig. 4.17a show a Vernier-like effect with the more superficial oxazine molecules reacting with the ammonia and locally altering the refractive index of the cavity. However, after the LIG inscription the fringes lost a lot of intensity, which may indicate that this intervention was quite destructive for the interferometer.

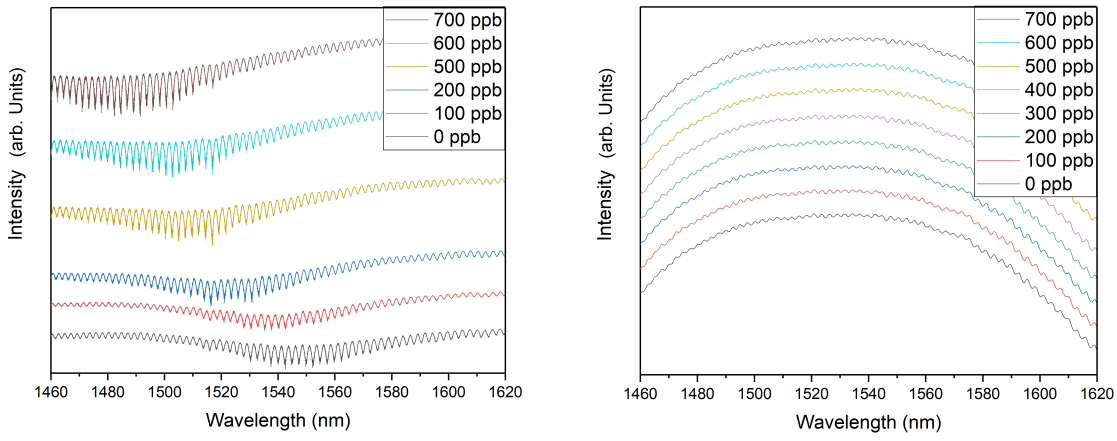

Figure 4.17: Ammonia tests for FP8 interferometer (a) before and (b) after LIG inscription.

In the graph of fig. 4.18 and table 4.5 are presented the FP8 and FP10 sensibilities for ammonia, as is possible to observe, the FP8 interferometer before the inscription of LIG shows some linearity and a sensitivity of -80±10 nm/ppm, almost 20 times higher than that reported in [63]. However, after the inscription of LIG, FP8 does not show a notable sensitivity, this indicates that the interferometer changes induced by the laser did not favor the detection of ammonia. A possible explanation for this could be that as oxazine is an organic material, it vaporizes when laser radiation hits it. The interferometer loses affinity for the ammonia and therefore loses a lot of sensitivity. Also, the sensitivity recorded for FP10 is not noteworthy, as expected. These results are still preliminary, so more tests need to be done to understand what kind of changes are induced by the laser and if oxazine has any influence on this, as it seems to have. However, it should be noted that the results are very promising for the detection of ammonia.

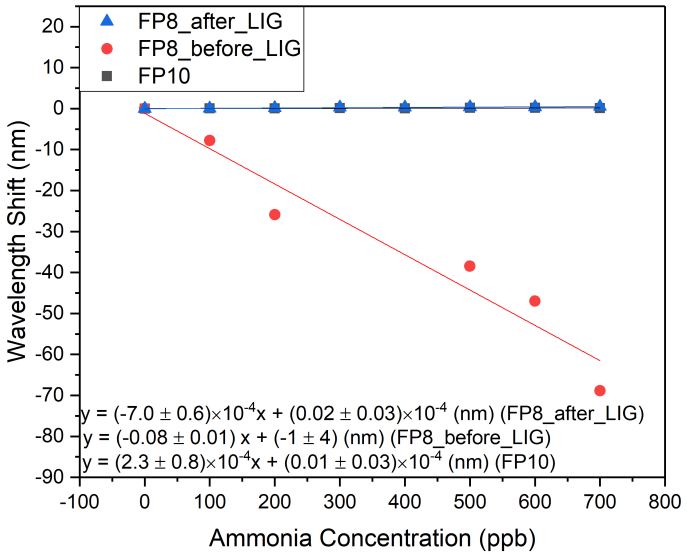

Figure 4.18: Ammonia tests for FP8 before and after LIG inscription and FP10.

Table 4.5: FP8 and FP10 gap, gap material, last procedure, and sensibilities for ammonia.

	Gap (μm)	**Gap Material**	**Last Procedure**	**Ammonia Sensibility (nm/ppm)**
FP8	195	PI	Gap Filling	-80
		Oxazine	LIG Inscribing	-0.7
FP10	231	PI	Gap Filling	0.23

— 5 —

Conclusions and Future Work

In this work, novel sensors were developed to potentially detect and monitor critical analytes present in aquaculture water. Cortisol and ammonia play an important and vital role in assessing the conditions in which crops live. At high concentrations, the presence of cortisol is associated with poor water quality, overcrowding or infections, and diseases. On another hand, ammonia in high concentrations causes eutrophication of the water, altering the ideal conditions for the healthy development of crops.

The development of the sensors had three distinct parts: the construction of an interferometer based on a Fabry-Pérot cavity, the transformation of part of the polyimide into laser-induced graphene, and finally the application of the interferometer in the detection of cortisol and ammonia.

In the first phase, the interferometers were constructed with the Fabry-Pérot cavity having been filled with and without the addition of gold nanoparticles to the base polyimide and were subsequently tested for strain, temperature, and refractive index. Due to the distending forces caused by the strain test, a second cavity was formed, making it impossible to use the interferometer as a strain sensor. Relatively, the temperature response and the RI the sensors demonstrated poor performance when compared with others of the same genre. Sensitivities recorded were at most -136 pm/°C and 40 nm/RIU to temperature and RI, respectively however, the addition of the nanoparticles to the polyimide increased the sensitivity to RI which is quite interesting. Furthermore, interferometers were constructed with a mixture of oxazine 170 perchlorate and polyimide for ammonia detection.

Secondly, various laser irradiation parameters were tested on polyimide-coated fiber to transform part of the polyimide into LIG. Keeping the pulse frequency at 20 kHz, different samples in which the power and the inscription speed were varied were analyzed by Raman spectroscopy, FTIR, and SEM-EDS. It was concluded that the produced LIG shows a high porosity, has a leafy texture and that sheets are composed of 10 or fewer layers of graphene. Also, when compared with other works, the LIG homogeneity is higher due to the pulsed laser used. Furthermore, for scanning speeds less than or equal to 100 mm/s the entire polyimide coating was transformed into LIG. From Raman spectroscopy, FTIR and SEM-

EDS were chosen 10% power and 100 mm/s inscription speed for the LIG inscription on the interferometers. After being subjected to the laser, the FPI spectral signals presented a drastic change, and the Vernier effect was achieved due to the appearance of a new cavity made of LIG inside the interferometer. It was observed that this change improved the refractive index sensitivity of the sensor up to 153 times.

Finally, interferometers were applied to the detention of cortisol and ammonia. For the first case, the interferometers were functionalized to achieve affinity towards cortisol. After each functionalization step, the interferometer spectrum was acquired showing deviations in the Vernier envelope, being a good indication regarding the immobilization of the antibody on the surface of the LIG. After functionalization, the interferometers were tested at different cortisol concentrations showing a sensitivity of -4.1±0.2 nm/log(ng/mL) and -34±5 nm/log(ng/mL). The presence of AuNPs in the last interferometer appears to increase cortisol sensitivity. Compared to the non-functionalized interferometers, these values obtained were substantially higher. To verify the immobilization of the antibody on the LIG surface, FTIR analysis was performed and allowed to observe the appearance of vibration bands associated with the functionalization process, proving the immobilization of the antibody successfully. For the selectivity and response to pH variations, the sensor proved to be quite immune to other substances, but due to its high sensitivity to refractive index, it was also sensitive to pH variation. In the case of ammonia detection, sensors with and without the formation of LIG in their cavities were tested. It was observed that the formation of LIG was quite destructive for the sensor, however, it was possible to obtain sensitivities of -80±10 nm/ppm in interferometers that were not subjected to the laser.

During the development of interferometers, it was noted that the penetration of the LIG into the cavity depended on the thickness of the interferometer and influenced the intensity of the spectra. For future work, it would be interesting to homogenize the manufacturing process by deposition of the polyimide in a controlled way. Also, the cavity length should be controlled through an automatic system to improve the consistency of the manufacturing process. Besides this, it was also tested the use of fibers already coated with polyimide, instead of the used acrylate-coated ones, however, the removal of the polyimide, through carbonization, necessary to prepare the fiber, left undesired residues and made its use impossible. Again, it would be useful to find a solution to be able to use this type of fiber.

Furthermore, the presence of AuNPs in PI increased the sensitivity to RI, this effect should be further studied. Even more interesting was the fact that the presence of the AuNPs in the polyimide also increased cortisol sensitivity by almost ten times. In this case, the influence of heat treatment and laser irradiation should be studied to understand the behavior of the AuNPs and whether they are aggregating or not, since it may have an influence on the detection as it occurs in Localized Surface Plasmon Resonance (LSPR) phenomena. To study this aggregation effect, high resolution SEM and absorbance measurements can be a powerful tool for this purpose.

Regarding the cortisol and ammonia sensors, although they have shown to be very promising detectors, it is necessary to repeat the tests and check the repeatability of the

process. It is also necessary to study the effect of the formation of LIG in the destruction of ammonia sensors and the influence of oxazine in this process. For this purpose, one could try mixing different amounts of oxazine (such as 0.5 mg, 0.1 mg, or 0.05 mg) or even test inorganic compounds with an affinity for ammonia.

A next step could be to take advantage of the extraordinary electrochemical response of LIG to produce a multiparameter electrochemical/optical sensor. It has already been proven that it is possible to detect cortisol and ammonia optically, so it would be interesting to electrochemically detect other interest analytes using the LIG layer formed, as bacteria or even nitrates and/or nitrites [18].

References

[1] G. V. Research. "Meat, poultry and seafood market size, share trend analysis report by product (meat, poultry), by type (conventional, organic), by form (fresh, frozen), by distribution channel, by region, and segment forecasts, 2022 - 2030." (), [Online]. Available: `https://www.grandviewresearch.com/industry-analysis/meat-poultry-seafood-market`. (accessed: 23.11.2022).

[2] P. R. Hannah Ritchie and M. Roser. "Meat and dairy production." (), [Online]. Available: `https://ourworldindata.org/meat-production`. (accessed: 23.11.2022).

[3] H. Ritchie and M. Roser. "Fish and overfishing." (), [Online]. Available: `https://ourworldindata.org/fish-and-overfishing`. (accessed: 23.11.2022).

[4] C. I. Justino, K. R. Duarte, A. C. Freitas, T. S. Panteleitchouk, A. C. Duarte, and T. A. Rocha-Santos, "Contaminants in aquaculture: Overview of analytical techniques for their determination," *TrAC Trends in Analytical Chemistry*, vol. 80, pp. 293–310, 2016.

[5] C. Cháfer-Pericás, Á. Maquieira, R. Puchades, B. Company, J. Miralles, and A. Moreno, "Multiresidue determination of antibiotics in aquaculture fish samples by hplc–ms/ms," *Aquaculture Research*, vol. 41, no. 9, e217–e225, 2010.

[6] L. Ranjbar, Y. Yamini, A. Saleh, S. Seidi, and M. Faraji, "Ionic liquid based dispersive liquid-liquid microextraction combined with icp-oes for the determination of trace quantities of cobalt, copper, manganese, nickel and zinc in environmental water samples," *Microchimica Acta*, vol. 177, no. 1, pp. 119–127, 2012.

[7] J. van Rijn and G. Rivera, "Aerobic and anaerobic biofiltration in an aquaculture unit—nitrite accumulation as a result of nitrification and denitrification," *Aquacultural engineering*, vol. 9, no. 4, pp. 217–234, 1990.

[8] A. E. Murphy, I. C. Anderson, A. R. Smyth, B. Song, and M. W. Luckenbach, "Microbial nitrogen processing in hard clam (mercenaria mercenaria) aquaculture sediments: The relative importance of denitrification and dissimilatory nitrate reduction to ammonium (dnra)," *Limnology and Oceanography*, vol. 61, no. 5, pp. 1589–1604, 2016.

[9] A. Ciji and M. S. Akhtar, "Nitrite implications and its management strategies in aquaculture: A review," *Reviews in Aquaculture*, vol. 12, no. 2, pp. 878–908, 2020.

[10] A. G. Leal-Junior, A. Frizera, and C. Marques, "Low-cost fiberoptic probe for ammonia early detection in fish farms," *Remote Sensing*, vol. 12, no. 9, p. 1439, 2020.

[11] C. Leitão, A. Leal-Junior, A. R. Almeida, *et al.*, "Cortisol aupd plasmonic unclad pof biosensor," *Biotechnology Reports*, vol. 29, e00587, 2021.

[12] J. Bly, S. Quiniou, and L. Clem, "Environmental effects on fish immune mechanisms.," *Developments in biological standardization*, vol. 90, pp. 33–43, 1997.

[13] M. W. Davis, "Fish stress and mortality can be predicted using reflex impairment," *Fish and Fisheries*, vol. 11, no. 1, pp. 1–11, 2010.

[14] S. Yin, P. B. Ruffin, and T. Francis, *Fiber optic sensors*. CRC press, 2017.

[15] S. Young, D. Penumadu, D. Foster, *et al.*, "Smart adhesive joint with high-definition fiber-optic sensing for automotive applications," *Sensors*, vol. 20, no. 3, p. 614, 2020.

[16] E. P. Randviir, D. A. Brownson, and C. E. Banks, "A decade of graphene research: Production, applications and outlook," *Materials Today*, vol. 17, no. 9, pp. 426–432, 2014.

[17] G. Li, Y. Xia, Y. Tian, *et al.*, "Recent developments on graphene-based electrochemical sensors toward nitrite," *Journal of the Electrochemical Society*, vol. 166, no. 12, B881, 2019.

[18] R. A. Ribeiro, L. L. Ferreira, A. J. Fernandes, F. M. Da Costa, C. Marques, and N. F. Santos, "Laser-induced graphene on optical fibre: Towards simple and cost-effective electrochemical/optical lab-on-fibre bioplatforms," 2023.

[19] J. Ayto, "Dictionary of word origins," Arcade Publishing, Tech. Rep., 1990.

[20] M. Born and E. Wolf, *Principles of optics: electromagnetic theory of propagation, interference and diffraction of light*. Elsevier, 2013.

[21] J. Frercks, "Creativity and technology in experimentation: Fizeau's terrestrial determination of the speed of light," *Centaurus*, vol. 42, no. 4, pp. 249–287, 2000.

[22] G. R. Fowles, *Introduction to modern optics*. Courier Corporation, 1989.

[23] L. Salasnich, *QUANTUM PHYSICS OF LIGHT AND MATTER*. Springer, 2017.

[24] Y. Zhao, X.-g. Li, X. Zhou, and Y.-n. Zhang, "Review on the graphene based optical fiber chemical and biological sensors," *Sensors and Actuators B: Chemical*, vol. 231, pp. 324–340, 2016.

[25] J. C. Palais, "Fiber optic communications," *Englewood Cliffs*, 1984.

[26] D. Jain, M. A. George, B. Harris, and S. Fleming, "Approximate modal cut-off wavelengths and the v-parameter for m-type optical fibers and its novel applications," *Journal of Lightwave Technology*, vol. 39, no. 13, pp. 4478–4488, 2021.

[27] A. D. Kersey, "Multiplexed fiber optic sensors," *Distributed and Multiplexed Fiber Optic Sensors II*, vol. 1797, pp. 161–185, 1993.

[28] P. Wang, C. Jiang, H. Chen, *et al.*, "Fabry-pérot cavity based on polyimide cold-spliced and vernier effect for relative humidity sensing application," *Optik*, vol. 270, p. 169 971, 2022.

[29] M. Deng, C.-P. Tang, T. Zhu, and Y.-J. Rao, "Pcf-based fabry-perot interferometric sensor for strain measurement under high-temperature," in *21st International Conference on Optical Fiber Sensors*, SPIE, vol. 7753, 2011, pp. 152–155.

[30] L.-C. Xu, M. Deng, D.-W. Duan, W.-P. Wen, and M. Han, "High-temperature measurement by using a pcf-based fabry–perot interferometer," *Optics and Lasers in Engineering*, vol. 50, no. 10, pp. 1391–1396, 2012.

[31] M. S. Ferreira, P. Roriz, J. Bierlich, *et al.*, "Fabry-perot cavity based on silica tube for strain sensing at high temperatures," *Optics Express*, vol. 23, no. 12, pp. 16 063–16 070, 2015.

[32] P. A. Tafulo, P. A. Jorge, J. L. Santos, F. M. Araujo, and O. Frazao, "Intrinsic fabry–pérot cavity sensor based on etched multimode graded index fiber for strain and temperature measurement," *IEEE Sensors Journal*, vol. 12, no. 1, pp. 8–12, 2011.

[33] G. Zhang, M. Yang, and M. Wang, "Large temperature sensitivity of fiber-optic extrinsic fabry–perot interferometer based on polymer-filled glass capillary," *Optical Fiber Technology*, vol. 19, no. 6, pp. 618–622, 2013.

[34] D. Su, X. Qiao, Q. Rong, *et al.*, "A fiber fabry–perot interferometer based on a pva coating for humidity measurement," *Optics Communications*, vol. 311, pp. 107–110, 2013.

[35] X. Liu, M. Jiang, Q. Sui, and X. Geng, "Optical fibre fabry–perot relative humidity sensor based on hcpcf and chitosan film," *Journal of Modern optics*, vol. 63, no. 17, pp. 1668–1674, 2016.

[36] M. Islam, M. M. Ali, M.-H. Lai, K.-S. Lim, H. Ahmad, *et al.*, "Chronology of fabry-perot interferometer fiber-optic sensors and their applications: A review," *Sensors*, vol. 14, no. 4, pp. 7451–7488, 2014.

[37] A. D. Gomes, H. Bartelt, and O. Frazão, "Optical vernier effect: Recent advances and developments," *Laser & Photonics Reviews*, vol. 15, no. 7, p. 2 000 588, 2021.

[38] Y. Chen, L. Zhao, S. Hao, and J. Tang, "Advanced fiber sensors based on the vernier effect," *Sensors*, vol. 22, no. 7, p. 2694, 2022.

[39] J. Zhang, H. Liao, P. Lu, *et al.*, "Ultrasensitive temperature sensor with cascaded fiber optic fabry–perot interferometers based on vernier effect," *IEEE Photonics Journal*, vol. 10, no. 5, pp. 1–11, 2018.

[40] J. Li, M. Zhang, M. Wan, *et al.*, "Ultrasensitive refractive index sensor based on enhanced vernier effect through cascaded fiber core-offset pairs," *Optics express*, vol. 28, no. 3, pp. 4145–4155, 2020.

[41] R. Ferreira, T. Paixão, G. Lopes, M. F. Domingues, R. Oliveira, and P. Antunes, "Vernier effect-based optical fiber sensor for humidity and temperature monitoring," *IEEE Photonics Technology Letters*, vol. 33, no. 19, pp. 1061–1064, 2021.

[42] L. Malard, M. A. Pimenta, G. Dresselhaus, and M. Dresselhaus, "Raman spectroscopy in graphene," *Physics reports*, vol. 473, no. 5-6, pp. 51–87, 2009.

[43] A. C. Neto, F. Guinea, N. M. Peres, K. S. Novoselov, and A. K. Geim, "The electronic properties of graphene," *Reviews of modern physics*, vol. 81, no. 1, p. 109, 2009.

[44] X. Du, I. Skachko, A. Barker, and E. Y. Andrei, "Approaching ballistic transport in suspended graphene," *Nature nanotechnology*, vol. 3, no. 8, pp. 491–495, 2008.

[45] J.-W. Jiang, J.-S. Wang, and B. Li, "Young's modulus of graphene: A molecular dynamics study," *Physical Review B*, vol. 80, no. 11, p. 113 405, 2009.

[46] K. S. Novoselov, A. K. Geim, S. V. Morozov, *et al.*, "Electric field effect in atomically thin carbon films," *science*, vol. 306, no. 5696, pp. 666–669, 2004.

[47] K. Parvez, S. Yang, X. Feng, and K. Müllen, "Exfoliation of graphene via wet chemical routes," *Synthetic Metals*, vol. 210, pp. 123–132, 2015.

[48] K. De Silva, H.-H. Huang, R. Joshi, and M. Yoshimura, "Chemical reduction of graphene oxide using green reductants," *Carbon*, vol. 119, pp. 190–199, 2017.

[49] H. Fukidome, Y. Miyamoto, H. Handa, E. Saito, and M. Suemitsu, "Epitaxial growth processes of graphene on silicon substrates," *Japanese Journal of Applied Physics*, vol. 49, no. 1S, 01AH03, 2010.

[50] B. Deng, Z. Liu, and H. Peng, "Toward mass production of cvd graphene films," *Advanced Materials*, vol. 31, no. 9, p. 1 800 996, 2019.

[51] R. Ye, D. K. James, and J. M. Tour, "Laser-induced graphene," *Accounts of chemical research*, vol. 51, no. 7, pp. 1609–1620, 2018.

[52] A. Kaidarova and J. Kosel, "Physical sensors based on laser-induced graphene: A review," *IEEE Sensors Journal*, vol. 21, no. 11, pp. 12 426–12 443, 2020.

[53] R. K. Biswas, N. Farid, G. O'Connor, and P. Scully, "Improved conductivity of carbonized polyimide by co 2 laser graphitization," *Journal of Materials Chemistry C*, vol. 8, no. 13, pp. 4493–4501, 2020.

[54] A. Lamberti, F. Perrucci, M. Caprioli, *et al.*, "New insights on laser-induced graphene electrodes for flexible supercapacitors: Tunable morphology and physical properties," *Nanotechnology*, vol. 28, no. 17, p. 174 002, 2017.

[55] C. Teng, R. Min, J. Zheng, *et al.*, "Intensity-modulated polymer optical fiber-based refractive index sensor: A review," *Sensors*, vol. 22, no. 1, p. 81, 2022.

[56] L. Martins, B. Kulyk, A. Theodosiou, *et al.*, "Laser-induced graphene from commercial polyimide coated optical fibers for sensor development," *Optics & Laser Technology*, vol. 160, p. 109 047, 2023.

[57] X. Dong, H. Zhang, B. Liu, and Y. Miao, "Tilted fiber bragg gratings: Principle and sensing applications," *Photonic Sensors*, vol. 1, pp. 6–30, 2011.

[58] Z. Wang, R. Singh, C. Marques, R. Jha, B. Zhang, and S. Kumar, "Taper-in-taper fiber structure-based lspr sensor for alanine aminotransferase detection," *Optics Express*, vol. 29, no. 26, pp. 43 793–43 810, 2021.

[59] O. Krarup, C. Baker, L. Chen, and X. Bao, "Sensitivity enhancement of fiber optical polarimetric sensors using self-induced nonlinear phase modulation via the kerr effect," *Optics Express*, vol. 30, no. 9, pp. 13 985–13 993, 2022.

[60] M. S. Soares, M. Vidal, N. F. Santos, *et al.*, "Immunosensing based on optical fiber technology: Recent advances," *Biosensors*, vol. 11, no. 9, p. 305, 2021.

[61] C. Leitão, S. O. Pereira, N. Alberto, *et al.*, "Cortisol in-fiber ultrasensitive plasmonic immunosensing," *IEEE Sensors Journal*, vol. 21, no. 3, pp. 3028–3034, 2020.

[62] M. S. Soares, L. C. Silva, M. Vidal, *et al.*, "Label-free plasmonic immunosensor for cortisol detection in a d-shaped optical fiber," *Biomedical Optics Express*, vol. 13, no. 6, pp. 3259–3274, 2022.

[63] A. G. Leal-Junior, A. Frizera, and C. Marques, "High sensitive ammonia detection in water with fabry-perot interferometers," *IEEE Photonics Technology Letters*, vol. 32, no. 14, pp. 863–866, 2020.

[64] A. H. Jalal, J. Yu, and A. A. Nnanna, "Fabrication and calibration of oxazine-based optic fiber sensor for detection of ammonia in water," *Applied Optics*, vol. 51, no. 17, pp. 3768–3775, 2012.

[65] H. Yoon, J. Nah, H. Kim, *et al.*, "A chemically modified laser-induced porous graphene based flexible and ultrasensitive electrochemical biosensor for sweat glucose detection," *Sensors and Actuators B: Chemical*, vol. 311, p. 127 866, 2020.

[66] K.-H. Nam, M. Abdulhafez, E. Castagnola, G. N. Tomaraei, X. T. Cui, and M. Bedewy, "Laser direct write of heteroatom-doped graphene on molecularly controlled polyimides for electrochemical biosensors with nanomolar sensitivity," *Carbon*, vol. 188, pp. 209–219, 2022.

[67] N. F. Santos, S. O. Pereira, A. Moreira, *et al.*, "Ir and uv laser-induced graphene: Application as dopamine electrochemical sensors," *Advanced Materials Technologies*, vol. 6, no. 6, p. 2 100 007, 2021.

[68] N. T. Garland, E. S. McLamore, N. D. Cavallaro, *et al.*, "Flexible laser-induced graphene for nitrogen sensing in soil," *ACS applied materials & interfaces*, vol. 10, no. 45, pp. 39 124–39 133, 2018.

[69] A. D. da Silva, W. J. Paschoalino, and L. T. Kubota, "A simple, sensitive, and selective electrochemical aptasensor for cortisol based on rgo-aunps," *Electroanalysis*, e202200401,

[70] B. Sun, Y. Gou, Y. Ma, *et al.*, "Investigate electrochemical immunosensor of cortisol based on gold nanoparticles/magnetic functionalized reduced graphene oxide," *Biosensors and Bioelectronics*, vol. 88, pp. 55–62, 2017.

[71] M. Hou, N. Wang, Y. Chen, *et al.*, "Laser-induced graphene coated hollow-core fiber for humidity sensing," *Sensors and Actuators B: Chemical*, vol. 359, p. 131 530, 2022.

[72] Y. Gao and L. Torrente-Murciano, "Mechanistic insights of the reduction of gold salts in the turkevich protocol," *Nanoscale*, vol. 12, no. 4, pp. 2740–2751, 2020.

[73] M. Lu, H. Zhu, C. G. Bazuin, W. Peng, and J.-F. Masson, "Polymer-templated gold nanoparticles on optical fibers for enhanced-sensitivity localized surface plasmon resonance biosensors," *ACS sensors*, vol. 4, no. 3, pp. 613–622, 2019.

[74] R. F. Egerton *et al.*, *Physical principles of electron microscopy*. Springer, 2005, vol. 56.

[75] W. Zhou, R. Apkarian, Z. L. Wang, and D. Joy, "Fundamentals of scanning electron microscopy (sem)," in *Scanning microscopy for nanotechnology*, Springer, 2006, pp. 1–40.

[76] T. Lovejoy, Q. Ramasse, M. Falke, *et al.*, "Single atom identification by energy dispersive x-ray spectroscopy," *Applied Physics Letters*, vol. 100, no. 15, p. 154 101, 2012.

[77] J.-J. Feng, X.-X. Lin, S.-S. Chen, H. Huang, and A.-J. Wang, "Thymine-directed synthesis of highly branched gold-palladium alloy nanobrambles as a highly active surface-enhanced raman scattering substrate," *Sensors and Actuators B: Chemical*, vol. 247, pp. 490–497, 2017.

[78] R. Nemanich, G. Lucovsky, and S. Solin, "Infrared active optical vibrations of graphite," *Solid State Communications*, vol. 23, no. 2, pp. 117–120, 1977.

[79] F. Tuinstra and J. L. Koenig, "Raman spectrum of graphite," *The Journal of chemical physics*, vol. 53, no. 3, pp. 1126–1130, 1970.

[80] A. C. Ferrari, J. C. Meyer, V. Scardaci, *et al.*, "Raman spectrum of graphene and graphene layers," *Physical review letters*, vol. 97, no. 18, p. 187 401, 2006.

[81] A. C. Ferrari and D. M. Basko, "Raman spectroscopy as a versatile tool for studying the properties of graphene," *Nature nanotechnology*, vol. 8, no. 4, pp. 235–246, 2013.

[82] L. Wang, Z. Wang, A. N. Bakhtiyari, and H. Zheng, "A comparative study of laser-induced graphene by co2 infrared laser and 355 nm ultraviolet (uv) laser," *Micromachines*, vol. 11, no. 12, p. 1094, 2020.

[83] I. Childres, L. A. Jauregui, W. Park, H. Cao, Y. P. Chen, *et al.*, "Raman spectroscopy of graphene and related materials," *New developments in photon and materials research*, vol. 1, pp. 1–20, 2013.

[84] T. Nicolet and C. All, "Introduction to fourier transform infrared spectrometry," *Thermo Nicolet Corporation*, 2001.

[85] F. A. Settle, *Handbook Of Instrumental Techniques For Analytical Chemistry*. Prentice Hall, 1997, vol. 1.

[86] P. A. Hayes, S. Vahur, and I. Leito, "Atr-ftir spectroscopy and quantitative multivariate analysis of paints and coating materials," *Spectrochimica Acta Part A: Molecular and Biomolecular Spectroscopy*, vol. 133, pp. 207–213, 2014.

[87] M. Janotta, D. Rudolph, A. Kueng, *et al.*, "Analysis of corrosion processes at the surface of diamond-like carbon protected zinc selenide waveguides," *Langmuir*, vol. 20, no. 20, pp. 8634–8640, 2004.

[88] S. Devouge, J. Conti, A. Goldsztein, *et al.*, "Surface functionalization of germanium atr devices for use in ftir-biosensors," *Journal of colloid and interface science*, vol. 332, no. 2, pp. 408–415, 2009.

[89] S. Hong, J. Kim, S. Jung, J. Lee, and B. S. Shin, "Surface morphological growth characteristics of laser-induced graphene with uv pulsed laser and sensor applications," *ACS Materials Letters*, vol. 5, no. 4, pp. 1261–1270, 2023.

[90] M. Hu, Z. Yao, and X. Wang, "Characterization techniques for graphene-based materials in catalysis," *AIMS Materials Science*, vol. 4, no. 3, pp. 755–788, 2017.

[91] K. Panwar, M. Jassal, and A. K. Agrawal, "In situ synthesis of ag–sio2 janus particles with epoxy functionality for textile applications," *Particuology*, vol. 19, pp. 107–112, 2015.

[92] J. Novak, E. Stepanovska, P. Malinsky, *et al.*, "The catalytic, sensory and electrical properties of go, pi and plla implanted by low-energy copper ions," *Nuclear Instruments and Methods in Physics Research Section B: Beam Interactions with Materials and Atoms*, vol. 540, pp. 199–209, 2023.

[93] S. Bagdeli, A. H. Rezayan, R. A. Taheri, M. Kamali, and M. Hosseini, "Fret-based immunoassay using cdte and aunps for the detection of ompw antigen of vibrio cholerae," *Journal of Luminescence*, vol. 192, pp. 932–939, 2017.

[94] P. Pandey, S. Singh, S. K. Arya, A. Sharma, M. Datta, and B. D. Malhotra, "Gold nanoparticle-polyaniline composite films for glucose sensing," *Journal of Nanoscience and Nanotechnology*, vol. 8, no. 6, pp. 3158–3163, 2008.

[95] D. Mokoena, B. P. George, and H. Abrahamse, "Conjugation of hypericin to gold nanoparticles for enhancement of photodynamic therapy in mcf-7 breast cancer cells," *Pharmaceutics*, vol. 14, no. 10, p. 2212, 2022.

[96] H. N. Lavudi, S. Kottapalli, and F. M. Goycoolea, "Extraction and physicochemical characterization of galactomannans from dichrostachys cinerea seeds," *Food Hydrocolloids*, vol. 82, pp. 451–456, 2018.

[97] G. A. à. Kiki, R. M. Pop, O. Sabin, *et al.*, "Polyphenols from dichrostachys cinerea fruits anti-inflammatory, analgesic, and antioxidant capacity in freund's adjuvant-induced arthritic rat model," *Molecules*, vol. 27, no. 17, p. 5445, 2022.